Structural Studies of Alloyed and Nanoparticle Transition Metal Dichalcogenides by Selenium-77 Solid-State Nuclear Magnetic Resonance Spectroscopy

Scott L. Carnahan,[1,2,3‡] Eunbyeol Gi,[1,2,‡] Molly Wagner,[1,‡] Anuluxan Santhiran,[1,2] Elise Amerongen,[1,3] Hang Yin,[4] Jessica Q. Geisenhoff,[4] Sharifur Rahman,[1,2] Oleksandr Dolotko,[1] Ihor Z. Hlova,[1] Viktor P. Balema,[1,5] Emily A. Smith,[1,2] Alina M. Schimpf,[4,6] Javier Vela,*[,1,2] and Aaron J. Rossini*[,1,2]

[1]US DOE Ames National Laboratory, Ames, Iowa, USA, 50011

[2]Iowa State University, Department of Chemistry, Ames, IA, USA, 50011

[3]Department of Chemistry, St. Mary's University of Minnesota, Winona, MN, USA, 55987

[4] Department of Chemistry and Biochemistry, University of California, San Diego, La Jolla, CA, USA, 92093

[5]Department of Materials Science & Engineering, Clemson University, Clemson, SC, USA, 29634

[6]Program in Materials Science and Engineering, University of California, San Diego, La Jolla, CA, USA, 92093

[‡]Equal contribution authors.

*Authors to Whom Correspondence Should be Addressed:

Professor Aaron J. Rossini – arossini@iastate.edu

Professor Javier Vela – vela@iastate.edu

TOC Graphic Abstract

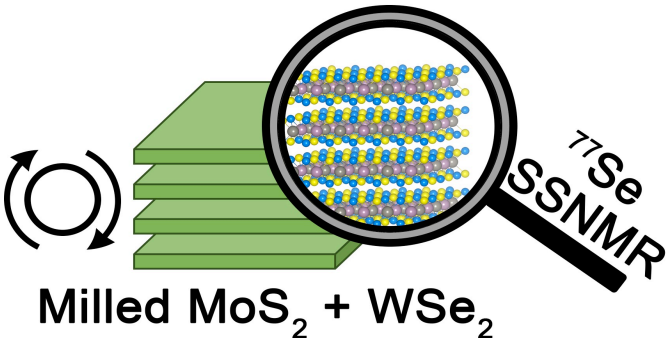

Abstract

Layered transition metal dichalcogenides (TMDCs) such as MoS_2, $MoSe_2$, and WSe_2 are under intense investigation because they are atomically thin semiconductors with photophysical properties that can be tuned by changing their composition or morphology. Mechanochemical processing has been proposed as a method to obtain alloyed TMDCs in the series $Mo_{1-x}W_xS_ySe_{2-y}$ (x = 0, 1; y = 0, 1, 2). However, elucidating the chemical transformations occurring at the atomic scale following mechanochemical processing can be challenging because the products are often amorphous. To address this challenge, we probe TMDC mixing and alloying by using a combination of powder X-ray diffraction (PXRD), optical (Raman) spectroscopy, ^{77}Se solid-state nuclear magnetic resonance (SSNMR) spectroscopy, and planewave density functional theory (DFT) calculations. The nature of the milling material and reaction atmosphere are shown to be essential factors in limiting the formation of undesired oxide byproducts. We demonstrate acquisition of ^{77}Se SSNMR spectra using different combinations of Carr-Purcell Meiboom-Gill acquisition (CPMG) pulse sequences, magic angle spinning (MAS), and MAS dynamic nuclear polarization (DNP). The combination of SSNMR with the other characterization methods demonstrates that high energy impact ball milling induces molecular level alloying of Mo, W and

chalcogen atoms in the family $Mo_{1-x}W_xS_ySe_{2-y}$. Gauge including projector augmented wave (GIPAW) DFT calculations yield accurate ^{77}Se chemical shift tensor components. ^{77}Se SSNMR spectroscopy was also applied to study the structure of WSe_2 nanocrystals intercalated with ethylenediamine. The intercalated WSe_2 nanocrystals exhibit a more positive isotropic ^{77}Se chemical shift as compared to bulk WSe_2, however, the ^{77}Se chemical shift anisotropy is the same, confirming the WSe_2 layers have a similar structure as in their bulk counterparts.

Introduction

Transition metal dichalcogenides (TMD or TMDCs) are 2D materials that generally have the unit formula MX_2, where M is a transition metal and X is S, Se, or Te (Figure 1a).[1,2] TMDCs consist of sheets made up of metal atoms and chalcogenides that are covalently bonded. Stacking of the sheets is driven by van der Waals forces. TMDCs have attracted considerable interest due to their few-atom-thin dimensions and interesting optical and electronic properties. There are several methods to obtain single-layered TMDCs.[3,4] TMDCs have a wide range of unique properties including tunable bandgap and intriguing quantum behavior.[5-7] One method of tuning the properties of TMDCs is to vary their composition by combining different chalcogens and transition metals in the same material. Until recently, the chemical preparation of single-phase mixed TMDCs in significant quantities was rather difficult.[8] Balema and co-workers reported a mechanochemical procedure to access the TMDC series $Mo_{1-x}W_xS_ySe_{2-y}$ (x = 0, 1; y = 0, 1, 2).[9] Mixing of $MoSe_2$ and WSe_2 in a planetary ball mill facilitated the exfoliation and mixing of these layered TMDC precursors. High-angle annular dark-field (HAADF-STEM) and scanning transmission electron microscope energy dispersive spectroscopy (STEM-EDS) appeared to indicate phase segregation of MS_2 and MSe_2 multi-layered slabs after milling in a planetary mill. Subsequent annealing of the processed samples was reported to lead to a homogeneous multi-element metals dichalcogens. One goal of the present work is to further investigate the alloying within samples of $Mo_{1-x}W_xS_ySe_{2-y}$ during mechanochemical processing, i.e., prior to the annealing. In this case, we used a SPEX 8000 mixer (impact) ball mill instead of the planetary one because impact milling provides higher energy that can facilitate the alloying of binary precursors. In order to investigate the structures of milled products we used powder X-ray diffraction (PXRD),

scanning electron microscopy (SEM) and energy dispersive X-ray (EDX) imaging, and ^{77}Se solid-state nuclear magnetic resonance (SSNMR) spectroscopy.

SSNMR spectroscopy is an ideal technique for the characterization of both crystalline and amorphous powdered solids, including those prepared by mechanochemical processes.[10,11] Therefore, SSNMR spectroscopy and could be a powerful probe of structure for TMDC materials. All of the elements within the $Mo_{1-x}W_xS_ySe_{2-y}$ series can potentially be studied by SSNMR spectroscopy. Recent reports have demonstrated acquisition of ^{95}Mo SSNMR spectra of MoS_2 at magnetic fields of 14.1 T and 35.2 T.[12,13] To the best of our knowledge, there are no reports of ^{183}W or ^{33}S SSNMR experiments on TMDC materials. ^{33}S is a low-abundance $I = 3/2$ nucleus that gives rise to broad quadrupolar powder patterns, making acquisition of ^{33}S SSNMR spectra challenging.[14] ^{183}W is a 14.3 % naturally abundant spin-½ nucleus that suffers from a low gyromagnetic ratio and long longitudinal relaxation time constants (T_1) which makes the observation of this nucleus challenging. In contrast, the NMR-active isotope of selenium, ^{77}Se is a spin-½ nucleus with a natural isotopic abundance of 7.6% and a gyromagnetic ratio that is 5.2 times smaller than the ^{1}H gyromagnetic ratio. ^{77}Se SSNMR spectroscopy has been applied to study elemental selenium,[15] inorganic selenides,[15-19] CdSe nanoparticles,[20-25] and organoselenium compounds.[18,26,27] ^{77}Se has a sizeable chemical shift range spanning more than 3000 ppm in diamagnetic solids. The large isotropic chemical shift range is advantageous because it can provide resolution between different selenium environments. However, large differences in isotropic chemical shifts and significant chemical shift anisotropy (CSA) can cause ^{77}Se NMR spectra to span breadths of hundreds or thousands of ppm.

Surprisingly, there are few reports of ^{77}Se SSNMR spectra of TMDC materials in the literature. A few studies have reported the ^{77}Se SSNMR spectra of paramagnetic or metallic

selenides such as $NbSe_2$, VSe_2, $TiSe_2$ and $TaSe_2$.[16,28-31] Due to the presence of unpaired electrons, these materials have relatively short ^{77}Se T_1 which enable routine acquisition of static ^{77}Se solid-state NMR spectra. To the best our knowledge, there are no prior ^{77}Se SSNMR studies of the diamagnetic TMDC materials WSe_2 or $MoSe_2$, apart from our recent paper which reported preliminary ^{77}Se MAS SSNMR spectra of WSe_2 in the context of probing the effects of grinding on the changes in crystallinity.[32]

In this work, we use a combination of PXRD, SEM, optical spectroscopy and ^{77}Se SSNMR spectroscopy to study the mixing and alloying of TMDCs in the family $Mo_{1-x}W_xS_ySe_{2-y}$ (x = 0, 1; y = 0, 1, 2). We employ PXRD to examine both the structural and compositional transformations of TMDC mixtures subjected to different ball milling and annealing conditions. We demonstrate that different combinations of Carr-Purcell Meiboom-Gill acquisition (CPMG) pulse sequences, magic angle spinning (MAS), and MAS dynamic nuclear polarization (DNP)[33-35] can be used for acquisition of ^{77}Se SSNMR spectra. To the best of our knowledge, this is the first study to systematically examine both pure and mixed TMDCs in the $Mo_{1-x}W_xS_ySe_{2-y}$ family by ^{77}Se SSNMR spectroscopy. We compare the experimental ^{77}Se SSNMR patterns with the chemical shift (CS) tensor parameters obtained from Density Functional Theory (DFT) calculations, which reveal the atomic environments and relative composition of the different selenium sites in the TMDCs. Finally, we also apply DNP-enhanced ^{77}Se SSNMR spectra to study the structure of ethylenediamine intercalated WSe_2 nanocrystals.

Results and Discussion

Possible Outcomes of Mechanochemical Processing of TMDCs. The mechanical processing of TMDCs may yield different results depending on the extent of mixing and alloying caused by various process conditions (Figure 1b). For example, physical mixing, using a mortar

and pestle or planetary mill for a limited period of time, results in well defined, phase segregated domains containing the fragments of the pure original binary TMDCs (Figure 1c). Alternatively, milling may produce hybrid heterostructures where slabs of different binary precursors are intermixed in a more or less random fashion (Figure 1d). More energy-intensive reaction conditions, for example, impact ball-milling followed by high-temperature treatment, can lead to the complete annoying of the starting materials into a new, atomically-ordered ternary or quaternary TMDCs (Figure 1e). Here, we assess the structure and elemental composition of different TMDC mixtures that were obtained by physical mixing, impact milling, and impact milling followed by annealing. We discern the structure of these materials using PXRD, energy dispersive X-ray spectroscopy (EDX) under a scanning electron microscope (SEM), optical absorption, Raman and ^{77}Se SSNMR spectroscopies. In particular, the latter technique is shown to provide clear insight into the mixing of TMDC phases induced by mechanochemical processing and/or annealing.

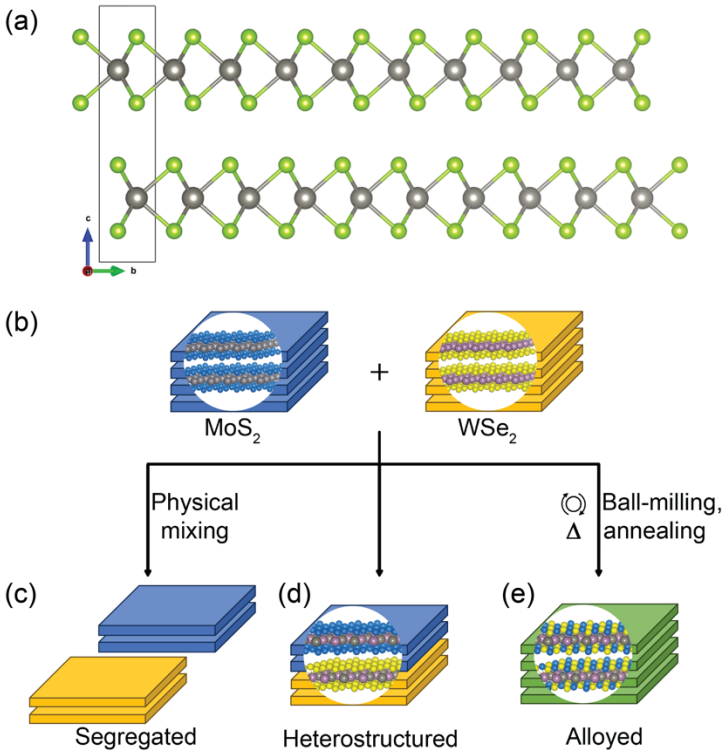

Figure 1. (a) Single crystal X-ray structure of MX_2 materials (M = Mo or W, grey atoms and X = S or Se, green atoms) for the 2H polytype (space group *P6₃/mmc*). (b) Depending on the conditions used, mixing two (or more) binary TMDCs may result in (c) segregated domains, (d) restacked, heterostuctured sheets, (e) or fully alloyed, ternary (or quaternary, etc.) TMDCs.

Powder X-ray Diffraction Analysis of Milled TMDCs. The PXRD patterns of pure and physically mixed TMDCs match their standard patterns (*P6₃/mmc*, Figure 2a and Table 1). As exemplified in the case of $MoSe_2$ and WSe_2, it is hard to distinguish these on the basis of PXRD alone, as the lattice parameters and individual reflections for these two TMDCs are close to one another – their (002) reflections appear at 2θ values of 13.7° and 13.6°, respectively. This difficulty underscores the need for using complementary techniques that fully probe the speciation of each metal chalcogenide site at the atomic level, such as ^{77}Se SSNMR spectroscopy.

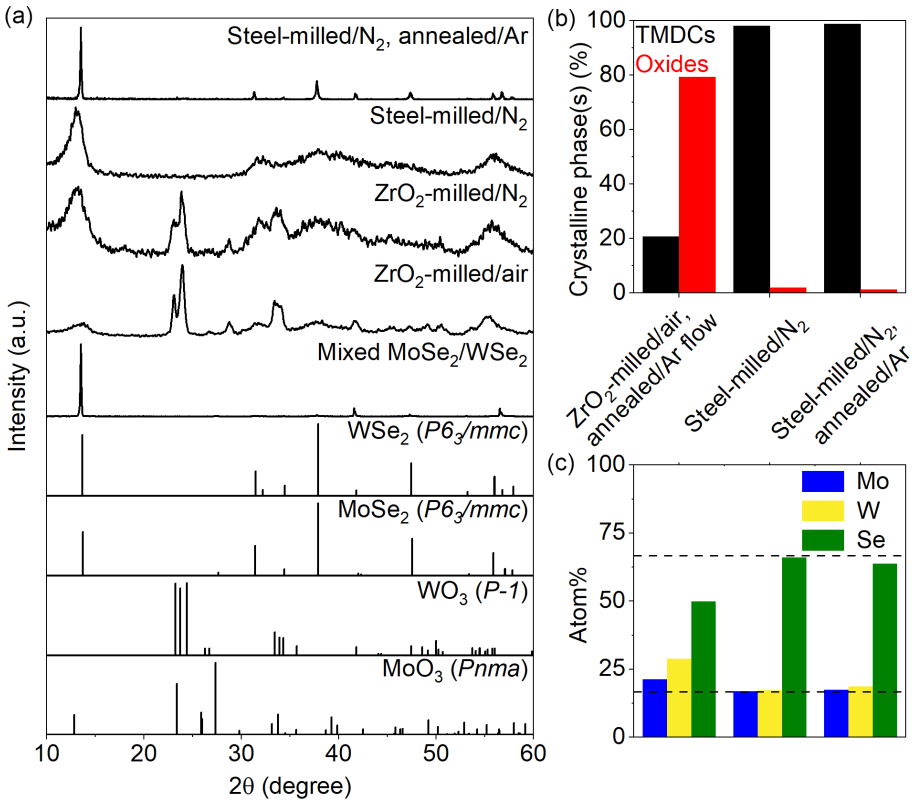

Figure 2. (a) Experimental PXRD patterns of mixed TMDCs with standard patterns of MoO_3 (#151750), WO_3 (#36168), $MoSe_2$ (#25391), and WSe_2 (#40752) from Inorganic Crystal Structure Database (ICSD). (b) The fraction of TMDC and oxide phases determined from PXRD using Match! (See Methods.). (c) Relative elemental composition analysis from SEM-EDX of mixed TMDCs samples prepared under different reaction conditions. Dotted guidelines in (c) correspond to the theoretical %atom values for each element.

Table 1. Conditions Used for Mixing and Alloying of TMDCs and Summary of PXRD Analysis.[a]

Precursors	Experimental conditions (ball-mill. and/or annealing)[a]	XRD phase(s) (%)	Scherrer size(s) (nm)[36,37,38]
$MoSe_2$ + WSe_2	None (physical mix.)[a]	$MoSe_2$, WSe_2	170±40
$MoSe_2$ + WSe_2	Annealed (1000 °C/Ar, 16 h)	$MoSe_2$, WSe_2	120±40[b]
$MoSe_2$ + WSe_2	Ball-mill (ZrO_2/air, 24 h)	MoO_3/WO_3 (86) TMDCs (14)	
$MoSe_2$ + WSe_2	Ball-mill (ZrO_2/air, 24 h), annealed (1000 °C/Ar flow, 16 h)	MoO_2/WO_2 (79) TMDCs (21)[b]	
$MoSe_2$ + WSe_2	Ball-mill (ZrO_2/N_2, 24 h)	MoO_3/WO_3 (29) TMDCs (71)	
$MoSe_2$ + WSe_2	Ball-mill (Steel/N_2, 24 h)	$Mo_{0.50}W_{0.52}Se_{2.0}$ (98)	12±2
$MoSe_2$ + WSe_2	Ball-mill (Steel/N_2, 24 h), annealed (1000 °C/Ar, 16 h)	$Mo_{0.53}W_{0.56}Se_{1.9}$ (99)	87±30
MoS_2 + WSe_2	None (physical mix.)[a]	MoS_2 (79) WSe_2 (21)	150±60 130±50
MoS_2 + WSe_2	Annealed (1000 °C/Ar, 16 h)	MoS_2 (40) WSe_2 (59)	130±40 110±20
MoS_2 + WSe_2	Ball-mill (Steel/N_2, 24 h)	$Mo_{0.49}W_{0.58}S_{0.91}Se_{1.0}$ (100)	14±3
MoS_2 + WSe_2	Ball-mill (Steel/N_2, 24 h), annealed (1000 °C/Ar, 16 h)	$Mo_{0.53}W_{0.54}S_{0.91}Se_{1.0}$ (100)	98±1

[a]All powdered samples were first physically-mixed at room temperature (RT = 21 °C) under air. Atmosphere is static (closed), unless noted otherwise ('flow'), see Methods. [b]See Supporting Information (SI) available.

Influence of processing conditions. The outcome of ball milling and/or annealing of the physically mixed TMDCs depends heavily on the specific equipment and reaction conditions used.[39] In particular, the use of zirconia balls or an air atmosphere leads to a high proportion of oxides, as determined by PXRD and SEM-EDX (Figure 2b–c, Table 1 and Figure S1). For example, milling a mixture of $MoSe_2$ and WSe_2 using ZrO_2 balls with an impact or "shaker" SPEX 8000M mill for 24 h under air results in 86% oxides, identified as MoO_3 and WO_3 (Figure 2a). Further annealing this mixture under a dynamic atmosphere of Ar (flow) only slightly reduces the proportion of oxides to 79%, in this case made mainly of MoO_2 and WO_2, possibly due to the formation and loss of volatile MO_x (M = Mo or W) species—see Supporting Information (SI).

To further probe the reasons behind these phenomena, we studied the effects of the ball milling material and the milling atmosphere separately. Specifically, a mixture of $MoSe_2$ and WSe_2 was packed into a zirconia jar loaded with ZrO_2 balls inside of an N_2 atmosphere. This setup

reduced the formation of oxides as compared to samples milled under air, however the fraction of crystalline oxides was still 29% (Figure 2a and Table 1). Zirconia jars are not as air-tight as steel jars and could leak during the milling process, explaining why oxide byproducts formed with the zirconia milling media. (Note that in all cases the milling equipment was located on the benchtop, see Methods.) Importantly, milling in hardened steel vials filled with N_2 atmosphere results in less than <2% oxides (Figure S2). Further annealing the mixtures obtained from the steel vials under a static Ar atmosphere inside a sealed quartz tube retained the high purity of the TMDC phases, with less than a 1% fraction of oxides as indicated by PXRD.

From physically segregated to alloyed TMDCs: Ball milling and annealing effects. Using the aforementioned, optimized reaction conditions— impact ball milling for 24 hours in a hardened steel vial packed under dry N_2, followed by annealing in a sealed quartz tube, under a static inert atmosphere—we followed the changes in the chemical speciation and dimensionality of the mixed TMDCs using structural and spectroscopic methods. Interestingly, a mixture of $MoSe_2$ and WSe_2 shows a much wider (002) reflection that is centered at a lower 2θ value compared to the reference TMDC patterns. We hypothesize the broadening of the (002) reflection arises from expansion and loss of ordering along the *c*-axis dimension upon milling. Furthermore, the single crystalline domain (Scherrer) sizes in the sample evolve upon milling and annealing, as evidenced by changes in the peak widths of the individual reflections observed by PXRD (Figure S3).

To gain a deeper understanding into these changes, we repeated the experiment starting with a mixture of MoS_2 and WSe_2, where the (002) reflections of the two TMDCs are much more easily resolved at 2θ values of 14.3° and 13.6°, respectively. As shown in Figure 3a, direct annealing without ball milling appears to have a negligible effect on the composition of the mixture, as evidenced form the presence of the two individual sets of reflections, corresponding to

MoS_2 and WSe_2, which are still clearly visible in the PXRD pattern of the heat-treated material (Table 1). In contrast, exhaustive (24 h) impact ball milling results in significant peak broadening of the XRD pattern, along with a shift in the (002) reflection to a lower 2θ value (as observed for the mixture containing $MoSe_2$ and WSe_2, see above and SI). Subsequent annealing of this milled sample generates a new single set of reflections with a narrower (002) peak at 13.8°, which is strong evidence for the formation of a new alloyed quaternary TMDC where the four elements are intimately mixed at the atomic level (Figure 3a). The initial broadening and shifting of the reflections in the as-milled sample can be attributed to several factors: a reduction in crystalline size, partial amorphization, and lattice strain. These factors introduce defects and dislocations into the crystal structure, which cause the reflections to broaden and shift in peak positions. Subsequent annealing decreases the lattice parameter *c*, indicating enhanced ordering, increased particle size, and improved crystalline structure.

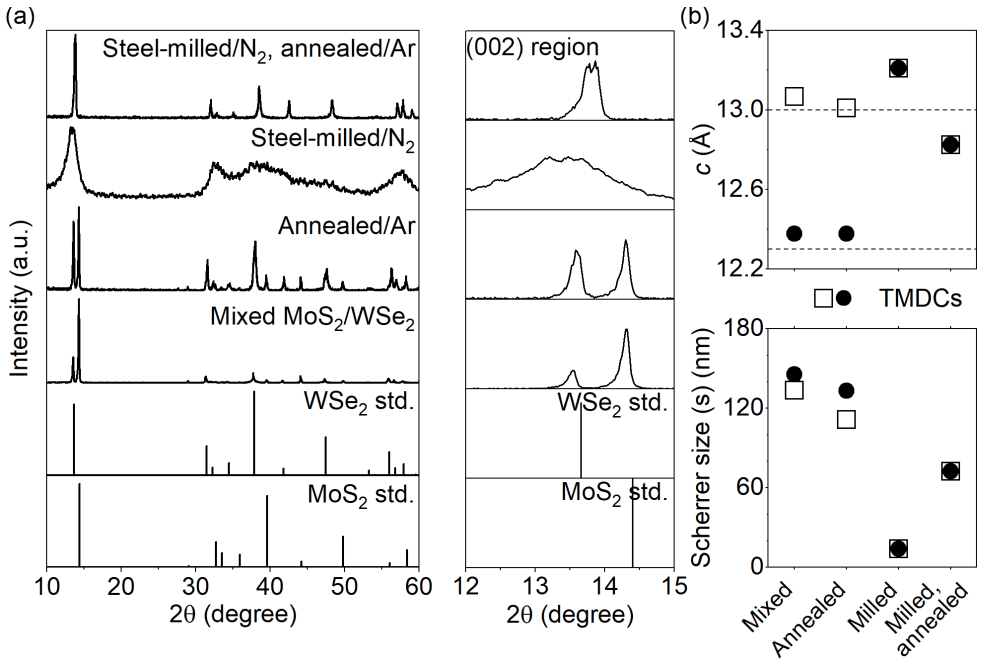

Figure 3. (a) Experimental PXRD patterns with standard patterns of MoS_2 (ICSD#49801) and WSe_2 (ICSD#40752). The right panel shows an expansion of the region where 002 reflections are visible. (b) *c* lattice parameter and apparent Scherrer size (● - MoS_2, □ - WSe_2, and when overlapped represents mixed TMDCs).

The number of (002) reflections in each PXRD pattern, along with their positions and widths—determined as their full width at half maximum (FWHM)—are a convenient indicator of the structural and chemical changes occurring in these samples. The physically mixed and the directly annealed samples both contain two distinct sets of reflections and hexagonal lattice parameters that closely match those of the pure binary MoS_2 and WSe_2 TMDCs, with specific *c* values of 12.2886(5) Å and 12.9860(9) Å, respectively (see SI).[40,41] In contrast, impact milling a mixture of MoS_2 and WSe_2 consistently and reproducibly resulted in a single set of PXRD reflections with a larger *c* value of *ca.* ~13.2 Å (see Methods and Figure 3a - insert). Similar shifts to smaller 2θ values and larger *c* parameters could suggest intercalation as was observed for TMDC

films deposited by vacuum filtration.[42] PXRD analysis of binary TMDCs obtained by planetary milling also showed larger *c* values due to intercalation-like reshuffling of binary precursors.[43] However, here we believe the observed increase in the interlayer distance after ball milling is due to uniaxial tensile strain across layers, as reported previously.[32,44] Indeed, subjecting the milled sample to thermal annealing, effectively removes such strain and disorder,[45] decreasing the *c* lattice parameter to 12.7355(15) Å, as determined by the Rietveld refinement (Table S1 and Figure S4). Because this last value is intermediate between those observed for the two original binaries, we can conclude that the extended impact ball milling followed by annealing effectively results in the formation of a new single quaternary TMDC alloy with the composition: $Mo_{0.53}W_{0.54}S_{0.91}Se_{1.0}$, as determined by EDX and ^{77}Se SSNMR spectroscopy (see below). The SEM-EDX elemental mapping shows the four elements are well mixed across both milled and milled and annealed samples (Figure S5-S8). In contrasts with the prior reports,[9] we did not observe the contamination of the samples with iron due to wearing out the steel milling balls and the vials during milling. Various factors such as the specific hardness of the milling materials as well as the brittleness of the research samples can all contribute to the possible degradation and decay of the milling media.[39,46] In our case, using only small-size milling balls along with lubricative behavior of MoS_2, $MoSe_2$ and WSe_2 may be responsible for very low levels of iron contamination, which fell below detection limits of the SEM-EDX analysis.

Examination of PXRD peak widths using a Scherrer constant (*K*) that is specific to layered materials[36,37] shows that the sizes of the single crystalline domains in the mixed TMDC samples across experiments range from *ca.* 14 to 150 nm (Figure 3b) We note that the Scherrer equation works best for estimating particle sizes less than 100–200 nm.[38] As shown in Figure 3b, the physical mixture shows the original binary TMDCs, MoS_2 and WSe_2 have domain sizes of 150±60

nm and 130±50 nm, respectively. Interestingly, direct annealing of this mixture—without ball milling—also shows very similar domain sizes at 130±40 nm and 110±20 nm. In contrast, impact ball milling for 24 h results in a significant decrease in the apparent particle size of the sample, which collapses to only 14±3 nm. Similar observations accompanied the interfacial reaction and alloying of several other nanoscale and soft materials, including mixed-halide perovskites[47] and cadmium chalcogenides.[48] Annealing the milled sample results in an increase in the Scherrer size to 98±1 nm, which can be explained by coalescence into larger alloyed domains.[47]

Optical monitoring of TMDC mixing. The electronic structure of TMDCs features direct and indirect band gaps depending on the number of stacking layers in the material. Monolayer (1L) TMDCs have direct band gaps,[49] while bulk or multilayer TMDCs have indirect band gaps.[50] For example, monolayer and bulk forms of MoS_2 feature 1.7 eV (direct) and 1.2 eV (indirect) band gaps,[51] respectively. In turn, monolayer and bulk forms of WSe_2 feature 1.4 eV (direct),[50] and 1.2 eV (indirect) band gaps,[52] respectively. Diffuse reflectance spectroscopy of pure binary TMDCs shows optical absorption onsets corresponding to the bulk form of the TMDCs between *ca.* 945–1030 nm (1.3–1.2 eV). Interestingly, another set of optical absorption onsets, likely corresponding to the direct band gap transition of a small population of monolayer to a few-layer-thick TMDCs in the bulk samples, appears at 715 nm (1.7 eV) and 895 nm (1.4 eV) for MoS_2 and WSe_2, respectively (see Figure S9 and Table 2). Because the direct band gap transition of TMDC is allowed, it seems reasonable to expect it to have a much larger cross section (extinction coefficient) than that for the indirect transition of a bulk TMDC.[53,54] Therefore, even a small number of monolayers may show up in the optical spectra of these materials.[55]

Raman Spectroscopy. We also applied Raman spectroscopy to monitor the structural changes occurring after impact milling (Figure 4). Layered TMDCs exhibit two first-order phonon modes

in the Raman spectrum. For example, bulk MoS_2 shows two bands at 378 cm^{-1} and 404 cm^{-1}, which correspond to E^1_{2g} (in-plane) and A_{1g} (out-of-plane) modes, respectively.[56] The E^1_{2g} and A_{1g} modes of bulk WSe_2 are unresolved as both appear at 247 cm^{-1}.[32] After exhaustive impact milling the mixture for 24 h, the characteristic bands from binary MoS_2 and WSe_2 disappear. Instead, two broad bands at 260 cm^{-1} and 327 cm^{-1} appear, consistent with an alteration of the phonon modes because of alloying into a quaternary phase. Specifically, the broad band at 260 cm^{-1} corresponds to a $MoSe_2/WSe_2$-like band, while the band at 327 cm^{-1} corresponds to a new Mo-W-S-Se vibration mode;[57] both of these bands are generated from a random distribution of elements in the alloyed TMDC.[58] Subsequent annealing of the milled sample results in the appearance of a new set of three broad bands at 262, 354, and 399 cm^{-1}. The broad feature at 262 cm^{-1} includes a $MoSe_2/WSe_2$-like A_{1g} mode, and the broad region at 354 cm^{-1} includes the MoS_2/WS_2-like E^1_{2g} mode, which arise from new S-Se interactions.[59] The band at 399 cm^{-1}, which corresponds to the A_{1g} mode of a MoS_2/WS_2-like structure, arises only after annealing of the milled sample. The appearance of the A_{1g} mode after annealing, which was absent after ball milling, indicates an increase in the layer thickness of the TMDCs.[57,60] This is consistent with PXRD analysis (above), which indicates the coalescence of sample grains into larger alloyed domains after annealing of the milled mixture.

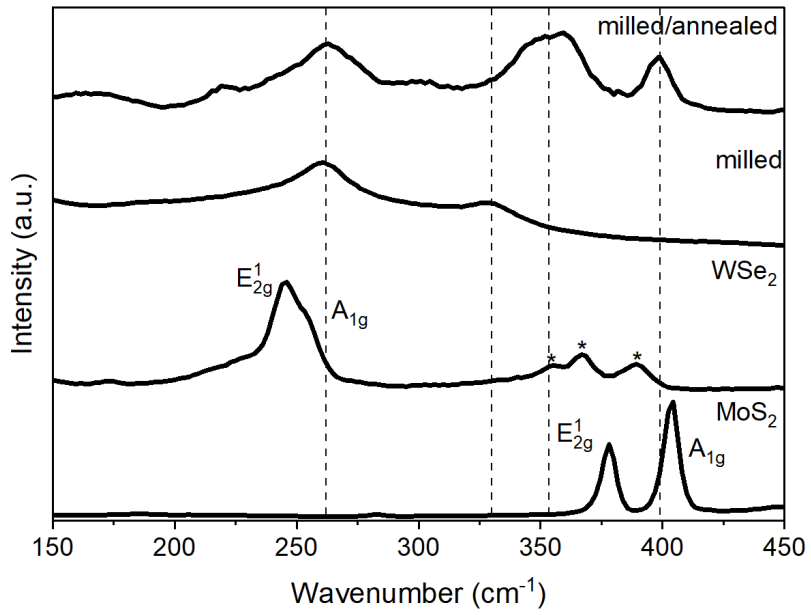

Figure 4. Raman spectra of pure MoS_2 and WSe_2 and milled mixtures (obtained with a 532 nm laser, * = multiphonon modes[61]).

^{77}Se solid-state NMR spectroscopy: Comparing acquisition methods. ^{77}Se SSNMR spectra of nanoparticles and organoselenium compounds are often obtained with cross-polarization magic angle spinning (CPMAS)[62] experiments.[63] ^{1}H{^{77}Se} CPMAS offers improved sensitivity compared to direct ^{77}Se excitation due to the signal gain provided by the higher polarization of ^{1}H spins. Additionally, ^{1}H T_1 are typically several magnitudes shorter than ^{77}Se T_1. When studying nanomaterials, ^{1}H{^{77}Se} CPMAS also selectively enhances the NMR signals of surface ^{77}Se spins that are nearest to organic ligands. For instance, ^{77}Se CPMAS was used to study the surface of CdSe nanoparticles and propose structural models of the surface termination.[24] Recently, dynamic nuclear polarization (DNP)[64,65,66,67] has been used to enhance the sensitivity of ^{77}Se CPMAS experiments on CdSe nanoparticles.[20,21] In inorganic materials such as selenides and TMDCs, there are typically no ^{1}H atoms in close proximity to ^{77}Se atoms to allow for CP transfer. Consequently, direct excitation ^{77}Se NMR experiments are required to study TMDC materials. As is discussed

below, these experiments can be time consuming due to ^{77}Se T_1 relaxation times which are on the order of tens of minutes.

Below, we first demonstrate how to acquire ^{77}Se SSNMR spectra of the pure TMDCs WSe_2 and $MoSe_2$. We show that CPMG techniques can provide large gains in sensitivity, enabling the routine acquisition of MAS and static ^{77}Se SSNMR spectra of WSe_2 and $MoSe_2$. We also investigate the use of DNP to accelerate ^{77}Se SSNMR experiments on WSe_2 and $MoSe_2$. Having established optimal methods to obtain ^{77}Se SSNMR spectra, we then turn to the study of mixed TMDC samples that were prepared by ball milling.

Static ^{77}Se SSNMR Experiments on WSe_2 and $MoSe_2$. We began with the acquisition of the static ^{77}Se SSNMR spectra of powdered $MoSe_2$ and WSe_2 (Figure 5). The ^{77}Se SSNMR spectra of pure $MoSe_2$ and WSe_2 were obtained with a direct excitation WURST-CPMG pulse sequence.[68,69,70,71] CPMG detection is estimated to improve sensitivity by one to two orders of magnitude because the samples have long homogeneous transverse relaxation times (T_2'). For example, for both $MoSe_2$ and WSe_2, echoes were visible after 1 second in the CPMG echo train (Figure S10). From fits of the echo intensities in the CPMG echo trains we estimate that the ^{77}Se T_2' values are greater than 0.5 s. One challenge in performing the direct excitation WURST-CPMG experiments is that the ^{77}Se T_1 were measured to be on the order of ten minutes in the pure TMDCs (Figure S11). Consequently, we found that recycle delays greater than 10 minutes yielded the best sensitivity for ^{77}Se solid-state NMR experiments on the pure TMDC materials. With CPMG detection we used 1000 s recycle delays and signal averaged 128 scans (35.6 hours) to obtain the high-quality ^{77}Se solid-state NMR spectra shown in Figure 5. The SSNMR spectra shown in Figure 5 were obtained with the samples packed into a 4 mm zirconia rotor and placed into a 5 mm transverse coil in a static NMR probe. The ^{77}Se saturation recovery experiments shown in Figure

S11 used samples packed into 5 mm glass solution NMR tubes. The 5 mm tubes hold approximately 2.5 times more sample as compared to the 4 mm zirconia rotors. With the 5 mm glass tubes we were able to obtain good quality ^{77}Se WURST-CPMG SSNMR spectra with averaging of only 4 to 8 scans and total experiment times of less than 1 hour (Figure S11).

MAS ^{77}Se SSNMR Experiments on WSe_2 and $MoSe_2$. We also performed MAS ^{77}Se solid-state NMR experiments. MAS narrows the broad static ^{77}Se powder patterns into well-resolved peaks. For the experiments on WSe_2 and $MoSe_2$ we used a 2.5 mm rotor and the CPMG pulse sequence with conventional rectangular ^{77}Se excitation and refocusing pulses. 32 scans and 128 scans were acquired for the ^{77}Se NMR spectra of $MoSe_2$ and WSe_2, respectively. A 1000s recycle delay was used for both compounds. The MAS CPMG ^{77}Se SSNMR experiments provide similar sensitivity to the static WURST-CPMG experiments, despite the fact that much smaller sample volumes were used in the 2.5 mm rotors. Note, the MAS ^{77}Se SSNMR experiments were performed with π refocusing pulses in the CPMG echo train, which typically provides ca. 50% larger signal intensity as compared to WURST refocusing pulses.[72] A 25 kHz MAS frequency is fast enough to nearly eliminate the spinning sidebands from the ^{77}Se NMR spectrum of WSe_2, while for $MoSe_2$ the sidebands are more intense due to the larger span of the ^{77}Se chemical shift tensor. For WSe_2 we also obtained MAS ^{77}Se SSNMR spectra in a 4 mm rotor with a 10 kHz MAS frequency (Figure S12). The 4 mm rotor holds approximately three times the sample volume of the 2.5 mm rotor. However, the ^{77}Se SSNMR spectrum obtained with the 2.5 mm rotor exhibited better sensitivity for the isotropic signal because the faster available MAS frequency helps to focus intensity into the isotropic peak.

In summary, MAS ^{77}Se CPMG SSNMR experiments were found to be effective for both $MoSe_2$ and WSe_2. Experiments on WSe_2 suggest that 2.5 mm rotors are preferred over 4 mm rotors

for MAS experiments because the faster available MAS frequencies increase the intensity of isotropic peaks, resulting in better sensitivity. Probes that use smaller diameter rotors are also advantageous because higher RF fields can be achieved, enabling more uniform excitation of broad sideband manifolds.

Determination of ^{77}Se Chemical Shift Tensor Parameters. Simulations of the MAS and static ^{77}Se SSNMR spectra allow for determination of the principal components of the chemical shift (CS) tensors ($\delta_{11} \geq \delta_{22} \geq \delta_{33}$), the isotropic chemical shift ($\delta_{iso} = (\delta_{11} + \delta_{22} + \delta_{33})/3$), and the anisotropic CS tensor parameters: the span ($\Omega = \delta_{11} - \delta_{33}$) and skew ($\kappa = 3[\delta_{22} - \delta_{iso}]/ \Omega$). The isotropic chemical shift values were determined from the MAS ^{77}Se SSNMR spectra, while the values of Ω and κ were determined by fitting the static SSNMR spectra. The values of these parameters are summarized in Table 2. The *ca.* 700 ppm difference in δ_{iso} for $MoSe_2$ and WSe_2 illustrates the sensitivity of ^{77}Se chemical shifts to the identity of the transition metal and the local selenium environment. Fits of the static ^{77}Se SSNMR spectra reveal that both $MoSe_2$ and WSe_2 show significant chemical shift anisotropy (CSA), with spans of 1090 ppm and 775 ppm for $MoSe_2$ and WSe_2, respectively. For both compounds the skew of the chemical shift tensor was –0.9 indicating that the ^{77}Se chemical shift tensors are axially symmetric within experimental error ($\delta_{22} \approx \delta_{33}$, corresponding to $\kappa \approx -1$). The symmetry of the chemical shift tensor is reflective of the symmetry of the selenium atoms. The selenium atoms reside in a trigonal pyramidal coordination environment, where they coordinate to three transition metals and have an open coordinate site that is presumably occupied by an electron lone pair.[73,74] Considering the symmetry of both the Se atoms and the CS tensor, δ_{11} must be aligned perpendicular to the planes of the 2D layers, while δ_{22} and δ_{33} reside in the plane. Indeed, this tensor orientation was predicted by DFT calculations (Figure S13).

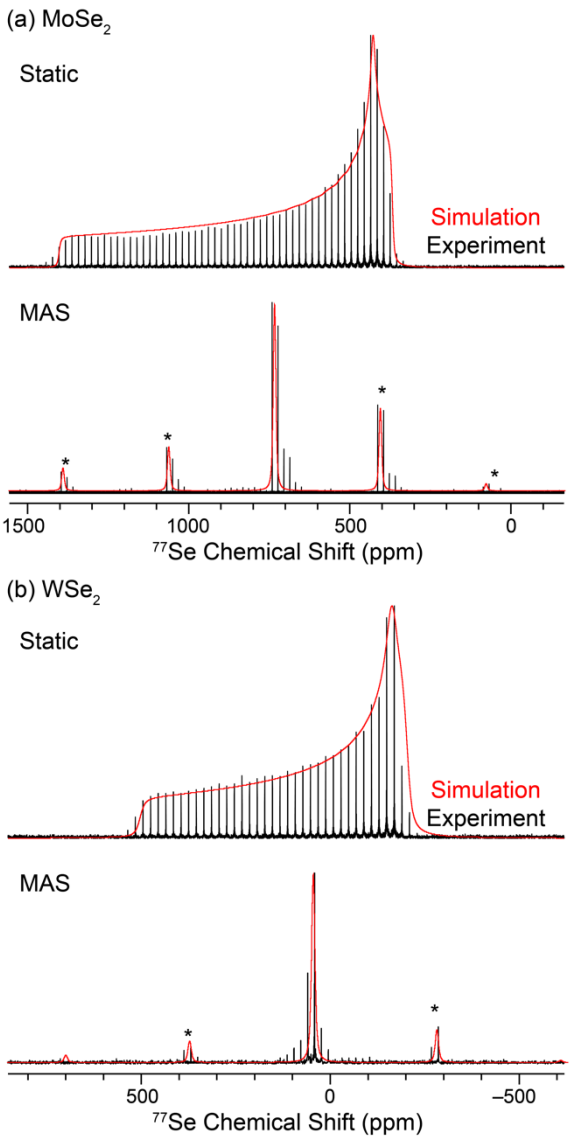

Figure 5. ^{77}Se direct excitation CPMG SSNMR spectra of (a) $MoSe_2$ and (b) WSe_2. Analytically simulated solid-state NMR spectra (red) are overlaid on the experimental CPMG SSNMR spectra (black). (Upper traces) Static ^{77}Se solid-state NMR spectra were acquired with the WURST CPMG pulse sequence using a transverse coil static probe and the sample held in a 4 mm zirconia rotor. For both WSe_2 and $MoSe_2$ 128 scans were acquired with a 1000 s recycle delay (35.6 hours total experiment time). (Lower traces) MAS NMR spectra were collected with a 2.5 mm MAS probe, a 25 kHz MAS frequency, and a CPMG pulse sequence that used rectangular pulses. For $MoSe_2$ and WSe_2, 32 scans and 128 scans were acquired, respectively, with a 1000 s recycle delay.

GIPAW Planewave DFT Calculations of ^{77}Se Chemical Shifts. Periodic planewave DFT gauge including projector augmented wave (GIPAW)[75,76,77,78] calculations were performed on WSe_2 and $MoSe_2$. Calculations were performed using both single-crystal X-ray diffraction

structures and fully relaxed (geometry optimized) crystal structures. The relaxation of the unit cell and atomic positions results in a minimal perturbation of the M-Se bond lengths and angles, however, there are slight changes in the interlayer spacing and *c*-axis (Figure S13). There is good agreement between calculated and experimental ^{77}Se CS tensor parameters if X-ray or relaxed atomic coordinates are used. All calculations predict that κ is –1.0, in good agreement with the experimental values of –0.9. Calculated isotropic chemical shifts show an average deviation of 12 ppm from the experimental shift (considering results on pure TMDC and mixed TMDC models). The calculated span for $MoSe_2$ is within 100 ppm of the experimental value. For WSe_2, the error in the span is on the order of 200 ppm. This observation is not surprising. W is heavier than Mo, meaning that spin-orbit contributions to the ^{77}Se chemical shielding will be more significant in WSe_2 than in $MoSe_2$. Spin-orbit effects are not accounted for in the GIPAW calculations we performed here, explaining the larger discrepancies in calculated CS tensor parameters for WSe_2. Finally, the DFT calculations confirm that in WSe_2 the CS tensor is oriented such that δ_{11} is perpendicular to the layers, while δ_{22} and δ_{33} are parallel to the layers (Figure S13).

Table 2. Experimental and Calculated ^{77}Se Chemical Shift (CS) Tensor Parameters.[a]

Compound	Se Site[b]	Method	δ_{iso} (ppm)	Ω (ppm)	κ	δ_{11} (ppm)	δ_{22} (ppm)	δ_{33} (ppm)
WSe_2	SeW_3	Experiment[c]	45	708	–0.9	503	–163	–207
	SeW_3	DFT X-ray[d]	65	474	–0.9	381	–93	–93
	SeW_3	DFT Optimized[e]	83	519	–0.9	429	–90	–90
	SeW_3	DFT Single Layer[f]	182	473	–0.9	498	25	25
$MoSe_2$	$SeMo_3$	Experiment	732	1035	–0.9	1402	427	367
	$SeMo_3$	DFT X-ray	749	1057	–0.9	1454	397	397
	$SeMo_3$	DFT Optimized	743	1025	–0.9	1427	402	402
$Mo_{0.5}W_{0.5}Se_2$ (milled and annealed)	SeW_3	Experiment[g]	63	651	–0.9	483	–126	–168
	SeW_3	DFT Optimized[h]	75	520	–0.9	417	–88	–103
	$SeMoW_2$	Experiment[g]	269	745	–0.6	714	124	–31
	$SeMoW_2$	DFT Optimized[h]	270	812	–0.4	742	138	–70
	$SeMo_2W$	Experiment[g]	492	930	–0.6	1052	302	122
	$SeMo_2W$	DFT Optimized[h]	481	1000	–0.5	1081	281	81
	$SeMo_3$	Experiment[g]	734	992	–0.9	1371	443	379
	$SeMo_3$	DFT Optimized[h]	732	1082	–0.9	1447	384	365

[a]GIPAW DFT calculated magnetic shielding values (σ_{jj}) were converted to chemical shift values (δ_{jj}) using the equation $\delta_{jj} = -1.16\sigma_{jj} + 1776$ ppm. See the calibration curve in Figure S12. [b]Se site indicates the identity of the three transition metal atoms that are covalently bonded to each Se atom. [c]Experimental values of δ_{iso} were determined from the MAS NMR spectra. Ω and κ were determined from fits of the static solid-state NMR spectra. All experimental values are from room temperature experiments. [d]Calculations were performed with atomic positions and unit cell parameters from X-ray crystal structures. [e]Calculations were performed with geometry optimization of atomic positions and unit cell parameters. [f]Calculations were performed with the inter-layer spacing increased so that there was 26.8 Å in between the Se atoms of adjacent layers. [g]Isotropic chemical shifts were measured from the MAS NMR spectrum of $Mo_{0.5}W_{0.5}Se_2$ and have uncertainties of less than 10 ppm. The values of Ω and κ were determined from fitting the static spectrum (Figure S17). Due to the peak overlap, the fitted values of Ω and κ have sizeable uncertainties on the order of 100 ppm and 0.4, respectively. [h]The calculated shielding values were averaged for all sites, then converted to chemical shifts for each type of site present in the super-cell model (Figure S12). Table S2 gives the principal components of the shielding tensor for each Se site.

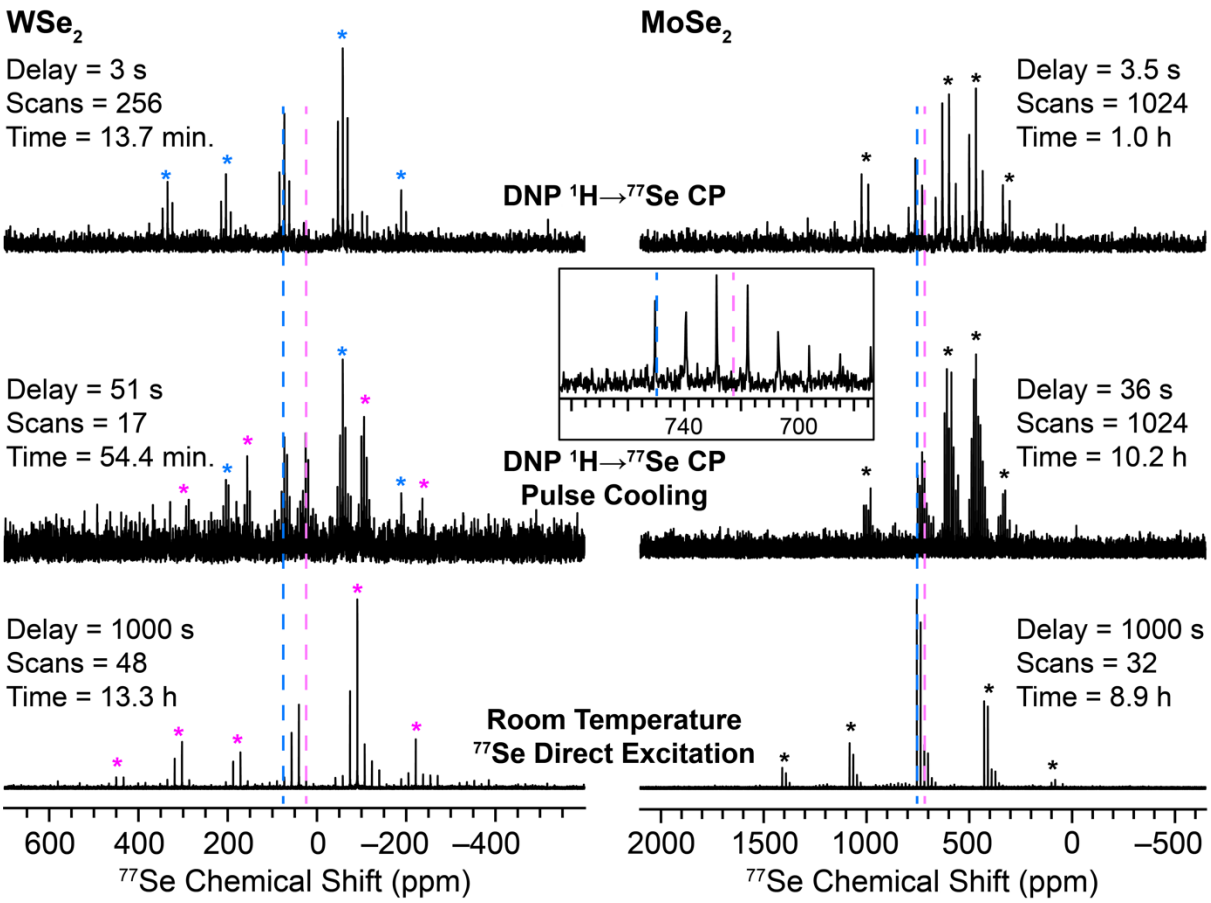

Figure 6. MAS ^{77}Se SSNMR of (left) WSe_2 and (right) $MoSe_2$. The NMR spectra were acquired with (upper) DNP and ^{1}H→^{77}Se CP, (middle) DNP ^{1}H→^{77}Se CP pulse-cooling, (lower) direct ^{77}Se excitation. Dashed lines are guides for the eye to illustrate the differences in isotropic chemical shifts. The inset shows an expansion of the isotropic peak region in the CP pulse-cooling spectrum of $MoSe_2$. The DNP experiments used a sample temperature of approximately 110 K, while the direct excitation NMR spectra were obtained at room temperature. The MAS frequency was 10 kHz in all cases, except for the room temperature direct excitation spectrum of $MoSe_2$ which was acquired with an MAS frequency of 25 kHz. CPMG detection was used in all cases. The pulse cooling experiments on WSe_2 and $MoSe_2$ used 17 and 12 ^{1}H→^{77}Se CP steps, respectively. Delays of 3 seconds were used in between the CP steps. The indicated recycle delays for pulse cooling experiments correspond to the total duration of the pulse cooling block.

MAS DNP ^{1}H-^{77}Se SSNMR Experiments on WSe_2 and $MoSe_2$. We also tested the feasibility of using MAS DNP to enhance the sensitivity of ^{77}Se SSNMR experiments on WSe_2 and $MoSe_2$. It is necessary to add an exogeneous polarizing agent solution to the TMDC materials to enable

DNP experiments. The established incipient wetness impregnation method was used to add the biradical solution to the TMDC materials.[79] Approximately 40 to 75 mg of TMDC material was impregnated with 10 μL of a 16 mM TEKPol 1,1,2,2-tetrachloroethane (TCE) solution.[80,81] In separate tests $MoSe_2$ was impregnated with different volumes of TCE solution. We observed that if too much TCE was added, the TMDC material would disperse or dissolve (Figure S14). We found that the best DNP enhancements were obtained for samples that had the consistency of wet, tacky powders.

We obtained ^{1}H spin echo NMR spectra of impregnated $MoSe_2$ and WSe_2 with and without microwave irradiation in order to estimate the ^{1}H DNP enhancement of the frozen TCE (ε_H, Figure S15). Based upon the intensity of ^{1}H spin echo NMR spectra, we measure ^{1}H DNP enhancements greater than 100 for both impregnated materials. The measured ε_H should indicate the approximate increase in ^{1}H spin polarization for the TCE molecules that coat the surface of the TMDC particles. As shown in Figure 6, with DNP we were able to obtain MAS ^{1}H→^{77}Se CP-CPMG SSNMR spectra in 13.7 minutes (256 scans) and 1.0 hour (1024 scans) for WSe_2 and $MoSe_2$, respectively. Without microwave irradiation we were unable to see any ^{1}H→^{77}Se CP-CPMG SSNMR signal for WSe_2 after acquisition of 64 scans (Figure S15). These observations suggest that the ^{1}H spins that participate in the ^{1}H→^{77}Se CP process had a similar DNP enhancement as the frozen TCE ^{1}H spins that are observed in the ^{1}H spin echo experiments.

Interestingly, the room temperature ^{77}Se solid-state NMR spectrum of WSe_2 shows an isotropic chemical shift of 45 ppm, while the DNP ^{1}H→^{77}Se CP-CPMG NMR spectrum shows an isotropic chemical shift of 73 ppm. In a ^{1}H→^{77}Se CP experiment, polarization can only be transferred to ^{77}Se spins that are within approximately 5 Å of the ^{1}H spins. Only the outer layers of TMDC sheets within a stack of sheets will be solvated by TCE molecules. Therefore, we

hypothesize that the chemical shift difference seen in the room temperature and DNP $^{1}H \rightarrow ^{77}Se$ CP-CPMG SSNMR experiments arises because this DNP ^{77}Se NMR spectrum is exclusively showing NMR signals from the outer TMDC sheets. This hypothesis also explains why the DNP SSNMR spectrum shows low signal-to-noise ratio. $^{1}H \rightarrow ^{77}Se$ CP will only be effective for the small fraction of ^{77}Se nuclei that reside on the outer layers of the TMDC crystals, resulting in a modest gain in sensitivity, despite the approximately hundred-fold gain in NMR signal intensity that should be realized from the combined effects of DNP and $^{1}H \rightarrow ^{77}Se$ CP. To support this hypothesis, we performed planewave DFT calculations on models of WSe_2 where we separated the layers of adjacent Se atoms by 26.8 Å of vacuum (Table 2). These calculations predict that removing the adjacent WSe_2 layers results in a 111 ppm increase in the isotropic chemical shift as compared to the X-ray crystal structure. The increase in predicted chemical shift is consistent with the more positive chemical shift seen in the experiments.

We also obtained the DNP ^{77}Se SSNMR spectra using the previously established DNP CP pulse-cooling experiment.[82,83,84] The pulse-cooling experiment has been demonstrated to enable the transfer of DNP-enhanced polarization into the core of inorganic solids that feature moderately abundant spin-1/2 nuclei. The CP pulse-cooling NMR spectrum of WSe_2 shows the same ^{77}Se peaks as were observed in the CP-CPMG NMR spectrum (blue dashed line, Figure 6), however, a second set of ^{77}Se sidebands with an isotropic peak at 26 ppm are also observed (pink dashed line, Figure 6). The intensity of the sidebands of for both peaks are similar, implying that the CS tensor parameters are similar for both Se sites. We assign the lower frequency set of ^{77}Se signals observed in the DNP CP pulse-cooling spectrum to bulk or core layers (i.e., layers that are surrounded by at least one other TMDC layer on both sides). The core ^{77}Se NMR signals in the CP pulse cooling spectrum (δ_{iso} = 26 ppm) are shifted from the room temperature direct excitation spectrum (δ_{iso} =

45 ppm) due to the differences in sample temperature. Direct excitation ^{77}Se MAS SSNMR spectra acquired at 110 K (without DNP) confirms that the isotropic peak is shifted to 26 ppm for WSe_2 (Figure S16).

For $MoSe_2$ the ^{77}Se isotropic chemical shifts are approximately 750 ppm and 732 ppm in the DNP CP-CPMG spectrum and room temperature direct excitation NMR spectrum, respectively. The CP pulse-cooling spectrum shows broader ^{77}Se NMR signals, with a second isotropic peak centered around 722 ppm. Again, this new, lower-frequency NMR signal observed in the CP pulse-cooling spectrum is assigned to NMR signals from the core layers of $MoSe_2$. The same chemical shift of 722 ppm is seen in a 110 K direct excitation ^{77}Se MAS SSNMR spectrum (Figure S16).

In summary, standard impregnation MAS DNP approaches can be used to attain modest sensitivity enhancements for ^{77}Se SSNMR experiments on WSe_2 and $MoSe_2$. Despite the large potential gains in sensitivity offered by DNP, the gains in sensitivity are limited by the fact that the ^{1}H→^{77}Se CP step will only excite NMR signals from the small fraction of Se atoms that reside on the outer layers of TMDC. The DNP ^{1}H→^{77}Se CP-CPMG SSNMR spectra show shifted signals as compared to the direct excitation ^{77}Se SSNMR spectra, which we attribute to the fact that ^{1}H→^{77}Se CP will only be effective for TMDC layers that are in direct contact with the solvent. DNP ^{1}H→^{77}Se CP pulse-cooling experiments result in the appearance of a second set of signals due to polarization transfer to core Se sites by homonuclear ^{77}Se spin diffusion. The core ^{77}Se NMR signals are shifted to lower frequency at 110 K as compared to their room temperature values.

Probing the atomic level alloying of TMDCs induced by ball milling using ^{77}Se solid-state NMR spectroscopy. Having established methods to acquire ^{77}Se SSNMR spectra of pure WSe_2 and

$MoSe_2$ we then turned to using ^{77}Se SSNMR spectroscopy to probe the atomic level structure of mixed TMDCs. For these experiments we studied the same set of mixed TMDCs which were studied by PXRD and optical spectroscopy: mixtures of WSe_2 and $MoSe_2$ or MoS_2 and WSe_2. We used room temperature MAS and static ^{77}Se SSNMR spectra to probe the local environment and monitor the atomic level mixing. Specifically, we looked at mixed TMDCs that were formed by physical mixing (ground by hand for less than 1 minute), physically mixed and annealed, impact ball milled mixtures, and then samples which were impact ball milled followed by an annealing step.

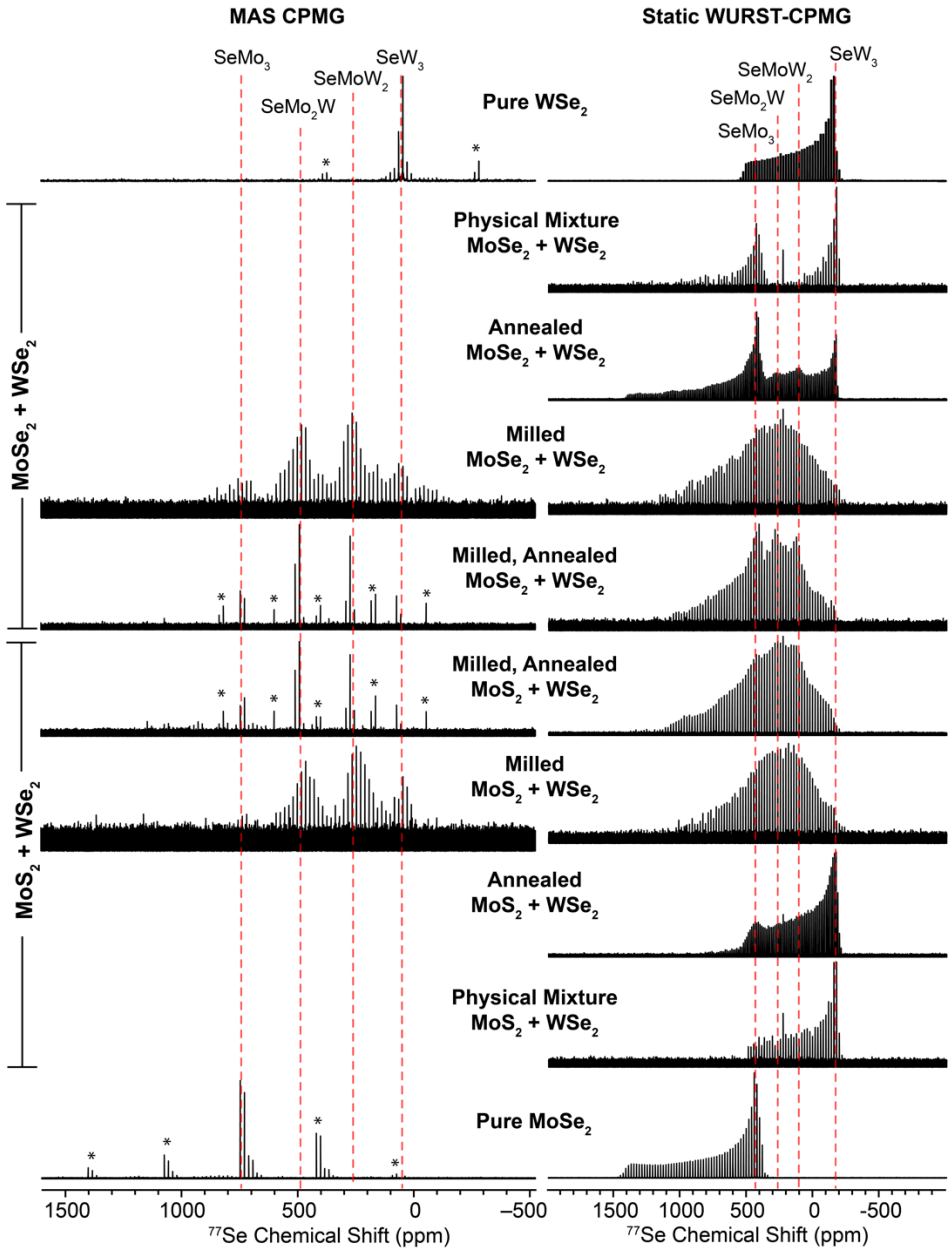

Figure 7. (left column) MAS CPMG and (right column) static WURST-CPMG ^{77}Se SSNMR spectra of pure TMDCs and mixtures of TMDCs prepared by physical mixing, annealing, impact milling, and milling followed by annealing. Dashed lines indicate isotropic chemical shifts on the MAS SSNMR spectra and the approximate position of δ_{22} on the static SSNMR spectra for each selenium site. All SSNMR spectra were obtained with direct ^{77}Se excitation at room temperature and with CPMG detection. All MAS experiments used a spinning frequency of 25 kHz.

The MAS CPMG and static WURST-QCPMG ^{77}Se SSNMR spectra of pure and the various mixed TMDCs are shown in Figure 7. From inspection of SSNMR spectra shown in Figure 7, it is immediately clear which mixing conditions can induce atomic level alloying of the two TMDCs. As expected, the static ^{77}Se WURST-CPMG SSNMR spectra of the physical mixtures show two distinct chemical shielding patterns for $MoSe_2$ and WSe_2, while for MoS_2 and WSe_2 only the WSe_2 pattern is visible because only this compound contains selenium. The ^{77}Se SSNMR spectra of annealed mixtures indicate there is minimal molecular level mixing of the TMDC materials, although there are some low intensity discontinuities at shifts of ca. 100 ppm and 200 ppm that could arise from partial exchange of W and Mo.

The MAS and static ^{77}Se SSNMR spectra of the milled and the milled and annealed samples show clear evidence of atomic level alloying of the constituent TMDCs. For all of the milled TMDC materials the two weakest isotropic signals occur at similar chemical shifts similar to those of the corresponding pure TMDC materials. On Figure 7, these shifts are denoted as $SeMo_3$ and SeW_3 because in $MoSe_2$ and WSe_2 each Se atom is bound to three Mo or W atoms, respectively (Figure 1). In the spectrum of the milled or milled and annealed samples there are two additional isotropic NMR signals at ca. 487 ppm and ca. 266 ppm that are assigned to Se atoms bound to 2 Mo and 1 W ($SeMo_2W$) and 1 Mo and 2 W ($SeMoW_2$), respectively. Planewave DFT calculations on a super-cell structure with overall composition $Mo_{0.5}W_{0.5}Se_2$ verifies the assignments of all NMR signals (Figure S13, Table 2 and Table S3). On Figure 7 we have indicated the isotropic ^{77}Se chemical shift on the MAS NMR spectra, while for static spectra we have indicated the approximate position of the δ_{22} as this discontinuity will be the most intense point of each shielding pattern. Based upon the observed isotropic chemical shifts it is possible to derive simple linear relationships relating the isotropic chemical shift to the number of Mo or W atoms bound to Se

(Figure S17). From fits of the static ^{77}Se SSNMR spectra, it is also possible to detect the mixing of the transition metal atoms (Figure S17). This is a helpful observation because equipment for static SSNMR experiments is likely available in more labs than equipment for MAS SSNMR experiments.

The MAS ^{77}Se SSNMR spectra show that the $SeMoW_2$ and $SeMo_2W$ NMR signals have approximately three times the intensity of the $SeMo_3$ and SeW_3 NMR signals in the milled materials. The relative peak intensities suggest that milling causes a random statistical mixing of Mo and W throughout the TMDC layers; there are three permutations that give $SeMoW_2$ and $SeMo_2W$ sites while $SeMo_3$ and SeW_3 sites can only be achieved in one configuration.

The milled materials possess much broader peaks in the MAS ^{77}Se SSNMR spectra than were seen in the annealed or starting materials. The isotropic peaks of the milled materials are inhomogeneously broadened with peak width at half height of around 100 ppm. The broadening likely reflects structural disorder that is caused by a distribution of inter-sheet spacings and distortions in the local M-Se bond angles and lengths due to damage caused to the structure by the milling process. The broadening of the NMR signals is consistent with the broadening of the diffraction peaks in the PXRD patterns (Figure 3a). Note, we have recently used EPR spectroscopy to detect stable paramagnetic centers that are present in milled TMDC materials.[85] These radicals likely correspond to unpaired electrons centered on Se or the transition metal ions that are created when the milling process causes lateral fractures in the TMDC particles. Consistent with the presence of paramagnetic centers in the milled materials, there is a significant reduction in both the ^{77}Se T_1 and T_2 in the milled materials (Figures S10 and S11). The reduction in the ^{77}Se T_2 and the limited number of CPMG spin echoes that can be acquired makes it more challenging to acquire the SSNMR spectra of the milled materials. EPR spectroscopy indicates that annealing eliminates

most of the paramagnetic centers created by milling. Consistent with this observation, the ^{77}Se T_1 and T_2 of the milled and annealed materials were similar to the pure TMDC materials. In addition, the narrowing of peaks upon annealing suggests an increase in atomic order, consistent with the narrowing of the reflections seen in the PXRD patterns of annealed material (Figure 3).

^{77}Se SSNMR spectroscopy of WSe_2 nanocrystals. Schimpf and co-workers have recently described methods to synthesize WSe_2 nanocrystals intercalated with ethylenediamine and trioctylphosphine.[86] Here, we applied ^{77}Se SSNMR to study WSe_2 nanocrystals with intercalated ethylenediamine. PXRD patterns show an increase of the interlayer spacing from 6.6 Å before intercalation to 10.2 Å after intercalation, indicating inclusion of ethylenediamine between the layers (Figure S18). Analysis of the PXRD diffraction peak widths suggest the nanocrystals have estimated lateral diameters of 13 nm and a thickness of 5 nm (Figure S18 and Table S4). Due to the challenges in extracting structural information about local structure from PXRD patterns or TEM images of the WSe_2 nanocrystals, we used ^{77}Se SSNMR to probe the local structure.

It was possible to synthesize the WSe_2 nanocrystals on ca. 20 mg scales. However, after losses during transfer and handling of the powdered materials we only had about 10 mg of sample. Given the small sample sizes, we used MAS DNP to obtain the ^{77}Se SSNMR spectra. Both DNP and ^{1}H→^{77}Se CP should be efficient on these materials due to the small size of the particles and the presence of the intercalated amines which should provide ^{1}H spins that can transport DNP enhanced polarization into the interior of the nanocrystals and also participate in CP. The sample for DNP was prepared by impregnating 10 mg of the WSe_2 nanocrystals with 5 μL of a TEKPol TCE solution. The sample was center packed in the rotor between powdered sodium chloride. Comparison of ^{13}C CPMAS solid-state NMR spectra acquired with and without microwave irradiation indicates that the DNP enhancement was 20 for the TCE solvent (peak at 74 ppm) and

ca. 4 for the amine CH_2 NMR signals (peaks at 45 ppm, Figure S19). Therefore, the DNP enhancement of the ethylene diamine ^1H spins inside the nanocrystals is likely only on the order of 4.

The modest ^1H DNP enhancement combined with limited sample quantity necessitated 13 hours of signal averaging (acquisition of 18432 scans) to obtain a reasonable quality $^1H \rightarrow ^{77}Se$ CP-CPMG spectrum. The MAS DNP ^{77}Se SSNMR spectrum of the amine intercalated WSe_2 nanocrystals shows a ^{77}Se isotropic chemical shift at 80 ppm and the sideband intensities indicate that the CS tensor parameters (Ω and κ) are similar to those measured for bulk WSe_2, confirming that the local structure of the Se atoms is similar to that seen in bulk WSe_2. However, the isotropic shift of 80 ppm for the nanocrystals is significantly different to chemical shift of 26 ppm seen for bulk WSe_2 at 110 K (using direct excitation MAS ^{77}Se CPMG experiments). The chemical shift of 80 ppm seen for the WSe_2 nanocrystals is similar to the chemical shift of 73 ppm that was observed in the DNP $^1H \rightarrow ^{77}Se$ CP-CPMG experiments on bulk WSe_2 (Figure 8c). Recall, we hypothesized that this shift occurred in bulk WSe_2 because the $^1H \rightarrow ^{77}Se$ CP-CPMG spectrum is primarily showing signal from outer TMDC sheets that are in direct contact with the TCE molecules. Therefore, it is perhaps unsurprising that the amine intercalated WSe_2 particles show a similar chemical shift because in this material all of the Se atoms will be in direct contact with ethylenediamine molecules. Note that the NMR signals from the nanocrystals exhibit significant inhomogeneous broadening (peak width at half height ca. 40 ppm). This broadening could arise from: (i) disordered, irregular packing of the intercalated ethylenediamine molecules in between the TMDC sheets and/or (ii) differences in ^{77}Se chemical shifts for Se atoms residing near or on the edges of the TMDC sheets and those residing within the center of the sheets or particles.

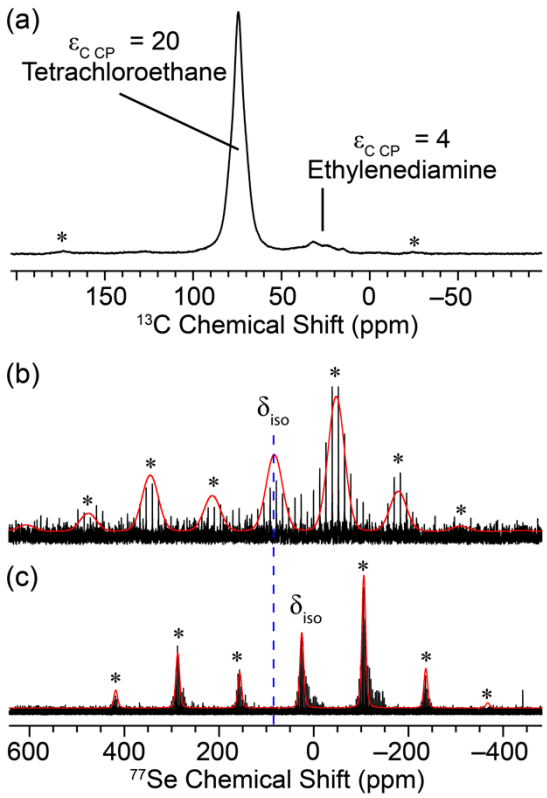

Figure 8. DNP-enhanced (a) $^{1}H \rightarrow ^{13}C$ CPMAS spectrum and (b) MAS $^{1}H \rightarrow ^{77}Se$ CP-CPMG spectrum of WSe_2 nanocrystals intercalated with ethylenediamine. (c) Direct excitation MAS CPMG ^{77}Se SSNMR spectrum of bulk WSe_2. All NMR spectra were recorded with a 10 kHz MAS frequency and a sample temperature of 110 K. Analytical simulations of the ^{77}Se SSNMR spectra are shown as red traces (parameters given in Table 2). The blue vertical dashed line indicates the ^{77}Se isotropic chemical shifts. The simulation of the ^{77}Se SSNMR spectrum of the WSe_2 nanocrystals used the same Ω and κ values as bulk WSe_2. Gaussian line broadening of 3000 Hz was used in the simulated spectrum of the WSe_2 nanocrystals to model the inhomogeneous broadening. Spinning sidebands are marked with an asterisk.

Conclusions

In conclusion, we have studied the mixing and alloying of TMDCs under various reaction conditions and followed these transformations at the atomic level using a combination of PXRD, SEM-EDX, and advanced ^{77}Se SSNMR spectroscopic methods. We find that the nature of the milling material and reaction atmosphere are essential factors in limiting the formation of undesired oxide byproducts. Routine PXRD is helpful in detecting atomic scrambling and alloying as long as the lattice parameters of two binary TMDCs are different enough, for example MoS_2 and WSe_2. However, routine PXRD alone is unable to detect the presence or extent of mixing or alloying, particularly when the original lattice parameters of the two original materials are close, such as in the case of $MoSe_2$ and WSe_2. Examination of PXRD reflection positions suggests that ball milling a mixture of TMDCs leads to a slightly larger stacking distance along the *c*-axis direction. Subsequent thermal annealing effectively removes this strain. Similarly, a close look at PXRD reflection widths reveals that the milling process decreases the single crystalline domain (Scherrer) size of the particles due to interfacial alloying of the two original TMDCs. Subsequent annealing increases the Scherrer size due to the coalescence of the alloyed features into larger domains.

We also established different techniques for acquiring the ^{77}Se SSNMR spectra of pure and mixed TMDCs. Static WURST-CPMG ^{77}Se SSNMR spectra of mixed and pure TMDC materials could be acquired in experiment times of hours to days. 2.5 mm rotors offered the best combination of sensitivity and resolution for MAS ^{77}SE SSNMR experiments. MAS DNP was also possible on the pure TMDC materials, however, DNP ^{1}H-^{77}Se CP-CPMG NMR spectra offered relatively low sensitivity and showed shifted signals, likely because these NMR spectra only show NMR signals from outer TMDC layers that are in contact with TCE. Hence, DNP could be of interest as a way

to investigate the surface modification of TMDC materials, however, it does not offer significant gains in sensitivity as compared to room temperature CPMG NMR experiments.

Both MAS and static ^{77}Se SSNMR spectra could easily be used to monitor the alloying of mixed TMDC materials. MAS ^{77}Se SSNMR spectra alloyed materials showed the appearance of signals at isotropic chemical shifts expected for Se atoms coordinated by 2 W/Mo and 1 Mo/W atoms, while the static ^{77}Se SSNMR spectra were a convolution of four shielding patterns arising from each unique Se environment. A correlation was seen between the broadening of peaks in the ^{77}Se NMR spectra and in the PXRD patterns. MAS DNP was used to obtain the ^{77}Se SSNMR spectra of ethylenediamine intercalated WSe_2 nanocrystals. The nanocrystals showed similar ^{77}Se CS tensor parameters to those seen in bulk WSe_2, confirming the preservation of the WSe_2 layered structural motif in the nanocrystals. A significant change in the ^{77}Se isotropic chemical shift was observed for the nanocrystals due to the presence of intercalated amines.

Future work should focus on using ^{77}Se SSNMR spectroscopy to study emerging layered selenide materials in both bulk crystalline and nanocrystalline forms. Another interesting direction would be to use ^{77}Se SSNMR to probe changes in surface structure that are thought to modify the photophysical properties of TMDC materials.

Methods

Materials. MoS_2 (98%) was purchased from Thermo Scientific, $MoSe_2$ (99.9%, metals basis) from Alfa Aesar, and WSe_2 (99.8%, 10−20 μm micron powder) from Alfa Aesar or BOC sciences. All materials were used as received. For nanocrystal synthesis and intercalation, tungsten hexacarbonyl ($W(CO)_6$, 99 %) was purchased from Acros, oleic acid (90 %) from Sigma Aldrich, trioctylphosphine oxide (99 %) from Strem, diphenyl diselenide (Ph_2Se_2 >97 %), hexadecane (98

%) and ethylenediamine (98 %) from TCI and methanol from Fisher Scientific. All chemicals were degassed using standard Schlenk techniques and stored in a nitrogen-filled glovebox.

Syntheses. General mixing and alloying procedure: Physical mixing. A 1:1 molar mixture of TMDCs was prepared by placing each binary—MoS_2 (0.638 g, 3.98 mmol) and WSe_2 (1.362 g, 3.98 mmol) or $MoSe_2$ (0.852 g, 3.36 mmol) and WSe_2 (1.148 g, 3.36 mmol) —in a 20 mL scintillation vial and vortexing the mixture for 10 s. *Ball-milling*. The mixture and milling balls were packed under either air or under an inert, dry N_2 atmosphere inside the glove box. We used two different sets of vials (also referred to as milling jars) and balls (see Table 1): (a) Zirconia vial (6.35 cm in diameter × 6.8 cm long), with three 12.7 mm diameter zirconia balls, and (b) hardened steel vial (5.7 cm in diameter × 7.62 cm long), with twelve 6.35 mm diameter steel balls (made of 52-100 steel from SPEXSAMPLEPREP). The sealed vials were then taken out and subjected to extended (24 h, 60 Hz, 1725 rpm) ball milling conditions with a SPEX 8000M shaker (impact) ball mill located on the bench top. *Annealing.* The sample was transferred to an oven-dried quartz tube, sealed, and annealed at 1000 °C for 16 h under a static atmosphere of inert dry N_2 or Ar. (Note: A static atmosphere inside a sealed ampule was necessary as control experiments showed that annealing in a tube furnace under a dynamic flow of Ar resulted in oxidation of the TMDCs.)

Structural characterization of bulk TMDC materials. The phase analysis and structural characterization of the starting materials and reaction products were carried out by powder X-ray diffraction analysis at room temperature on a Rigaku Ultima IV diffractometer (40 kV, 44 mA) using Cu-Kα radiation with a 0.02° 2θ step, in the range of Bragg angles 2θ from 5° to 60°. Quantification of TMDCs and oxides in PXRD patterns were estimated using the Reference Intensity Ratio (RIR) method[87] within Match!.[88] To calculate the *a* and *c* values from the PXRD patterns of mixed TMDCs, the 002 and 013 reflection peaks were fit to Gaussian curves in

OriginPro in order to extract the 2θ value.[89] The extracted 2θ values were then converted to *d*-spacing using the established equation for a hexagonal unit cell: $\frac{1}{d^2} = \frac{4}{3}\left(\frac{h^2+hk+k^2}{a^2}\right) + \frac{l^2}{c^2}$.

Rietveld Refinement. Rietveld refinement of select PXRD data was performed using the FullProf software package.[90] The peak profile shape was described by a pseudo-Voigt function. The background of the diffraction pattern was fitted using linear interpolation between selected data points in non-overlapping regions. The scale factor, lattice parameters, fractional coordinates of atoms and their isotropic displacement parameters, zero shift, profile shape parameters, and half-width (Caglioti) parameters were allowed to vary during the fitting. The least-square minimization showed systematic divergence when the M/X (M = Mo, W, and X = S or Se) occupations were treated as independent parameters in the obtained mixed TMDCs. To improve the stability of calculations, the occupation factors of all components were restrained to the compositions of the starting mixtures. Anisotropic broadening of (h 0 l) Bragg peaks due to the plate-like particle shapes is largely responsible for relatively high Rps.

Examination of PXRD peak widths using a Scherrer constant (*K*) that is specific to layered materials was used to estimate the size of single crystalline domain sizes under ≤200 nm.[36,37,38] SEM measurements on samples held on carbon tape were performed using a JEOL JSM-IT200. The detection limit for each element measured in the area scans is ± 0.1 wt%.[91] Representative SEM-EDX analyses of mixed TMDCs in Figure S8 lack evidence of additional elemental impurities.

Synthesis and intercalation of WSe_2 nanocrystals. The synthesis of WSe_2 nanocrystals was adapted from a previously reported method[86] and performed in duplicate to increase the yield. The masses used for each reaction are provided in Table S4. For each reaction, in a nitrogen-filled glovebox, tungsten hexacarbonyl ($W(CO)_6$; ~0.0200 g, 56.8 μmol), oleic acid (~1.6000 g, 5.6643

mmol), and tri-*n*-octylphosphine oxide (~5.0000 g, 12.932 mmol) were added to a 4-neck 25-ml round-bottom flask containing a Teflon stir bar. The flask was fitted with a rubber septum, two ceramic sheathes, and a condenser with a flow-adapter. Separately, in the glovebox, diphenyl diselenide (Ph_2Se_2; ~0.0710 mg, 0.227 mmol) and hexadecane (HDA; ~1.5460 g, 6.8283 mmol) were added to a 3-neck 25-ml round-bottom flask containing a Teflon stir bar. The flask was fitted with two rubber septa and a flow adapter. Both were transferred from the glovebox onto an argon-purged Schlenk line and were evacuated for 5 min and refilled with argon. This cycling process was repeated three times with the flow adapter closed and three more times with the flow adapter open. After cycling, the W-containing flask was stirred and heated to 320 °C using a proportional–integral–derivative controller with temperatures measured via a thermocouple inserted into a ceramic sheath. A different thermocouple connected to an Omega data logger was inserted into the other ceramic sheath to record the temperature during the reaction. Meanwhile, the Se-containing flask was stirred and heated to ~150 °C using a heating mantle connected to a variable transformer. When the W-containing flask reached 150 °C, 1 mL of the Ph_2Se_2/HDA solution was rapidly injected into the $W(CO)_6$ solution with an argon-purged 1-mL syringe and needle. The reaction continued to heat to a final temperature of 320 °C, after which it was held for 30 min. The heating mantle was then removed and the flask cooled to room temperature. After the contents of the flask solidified, the flask was evacuated and left under static vacuum to transfer into the glovebox. To each reaction, 5 mL toluene was added with mild heat (~60 °C) on a hotplate to resuspend the product (~15 min). The products were then transferred into two glass culture tubes and collected by centrifuging for 50 min at 4000 rpm. The products were subsequently washed twice by decanting the supernatants, adding 1 mL toluene and 1 mL MeOH to each tube, resuspending the pellets, and centrifuging for 30 min at 4000 rpm. The washed pellets were suspended in 2 mL

toluene and transferred into a scintillation vial containing a Teflon stir bar. From this stock solution, ~50 μL sample was removed and dried under vacuum for PXRD (Figure S18i), which revealed that the nanocrystal ensemble contains both the monoclinic *C*2/*m* (2M) and hexagonal P6$_3$/*mmc* (2H) phases of WSe_2. We note that precise phase-identification is challenging in nanocrystalline WSe_2.

To the remaining solution, 2.0188 g ethylenediamine was added and stirred at room temperature for 48 h. The product was split into two glass culture tubes and centrifuged for 20 min at 4000 rpm. The resulting pellet was resuspended in 1 mL toluene, from which ~50 μL was removed and dried under vacuum for PXRD (Figure S18ii). The shift of the (200) reflection to lower 2θ indicates an increase in the interlayer distance due to intercalation. The remaining ~950 μL was dried, yielding 19.7 mg of solid material, which was packed in a scintillation vial with a septum-lined cap for transportation.

PXRD on pre- and post-intercalated WSe_2 nanocrystals. The dried samples were removed from the glovebox immediately prior to measurement, which was conducted aerobically. PXRD was collected using a Cu-source diffractometer with a Bruker Apex II detector. For each measurement, a single pellet ~200 μm in diameter was picked out under a light microscope using a sample holder with a loop. Data was collected using three frames with a detector distance of 150 mm, spinning φ, and 120 s exposure time per frame. The frames were then merged and integrated with a γ range of 80–100° in Diffrac.eva and background subtraction was performed using a default curvature/threshold. The intensities in the ranges of 2θ = 5–15 ° and 30–32° were fit to Voigt functions using the lmfit package in python. The former contains the interlayer reflection ((200) in 2M, (002) in 2H) and provides a direct probe of the domain size along the stacking direction. The latter may contain many reflections ((−111) and (002) in 2M, (100) in 2H) and thus provides

only an estimate of the lateral size. Domain sizes were calculated using a modified Scherrer equation with $\kappa = 2$ and $c = -16$ Å. Instrument broadening was determined using a bulk lanthanum hexaboride standard, which was collected and analyzed as described above. Table S4 provides the fitted position (μ), full width at half maximum (FWHM), and corresponding domain sizes for WSe_2 nanocrystals before and after intercalation with ethylenediamine.

Optical and Raman Spectroscopy Characterization. Diffuse reflectance spectra were collected using an SL1 Tungsten Halogen lamp (vis−IR), an SL3 Deuterium Lamp (UV), and a BLACK-Comet C-SR-100 spectrometer (200−1080 nm). The band gap values were estimated by extrapolating the linear slope of Tauc plots by plotting $(Ahv)^{1/r}$ versus hv (A = absorbance, hv = incident photon energy in eV, and r = 1/2 for direct semiconductors and r = 2 for indirect semiconductors).[92,93] An XploRA Plus Raman confocal upright microscope (HORIBA Scientific, Edison, NJ) with a 532-nm solid-state diode laser running at 1.25 mW was used to collect Raman spectra. Raman spectra were obtained in the epi-direction using an Olympus objective (0.9 numerical aperture, 100× magnification). A 1200 gr/mm grating, a 300 μm monochromator slit, and a 100 μm confocal pinhole were used. Three accumulations were averaged for each measurement with a 120 s acquisition time, and three measurements were collected for three different locations. The Raman spectra were analyzed using the scientific analysis and graphing program Igor Pro ver. 6.37 (WaveMetrics, Inc., Lake Oswego, OR). Following background subtraction, peaks were fit using a Lorentzian function to determine the full-width-at-half-maximum and peak locations.

Room temperature SSNMR experiments. Room temperature SSNMR experiments were performed with a widebore 9.4 T magnet equipped with a Bruker Avance III HD console. Table S5 summarizes the pulse sequences, probe and key parameters used for acquisition of the different

NMR spectra. NMR data was processed using TopSpin software. Simulations of MAS and static NMR spectra were performed with the solid lineshape analysis (sola) module v2.2.4. For ^{77}Se direct excitation SSNMR experiments recycle delays between 50 s and 1000 s were used. Static SSNMR experiments were performed on a Bruker HX static probe with a 5 mm transverse coil. Static ^{77}Se SSNMR spectra were acquired with the WURST-CPMG pulse sequence.[69] The WURST pulses were 30 μs in duration, swept over a total frequency range of 600 kHz and the ^{77}Se RF field was approximately 66 kHz with an input power of 110 W. For the static WURST-CPMG experiments 4000 spin echoes were acquired, and each echo cycle was 1.050 ms in duration (including signal acquisition, ring down delays and pulses). For materials exhibiting shorter ^{77}Se T_2' such as the ball milled materials, the number of echoes was reduced during processing to increase the signal to noise ratio. MAS ^{77}Se SSNMR spectra were obtained with Bruker 2.5 mm or 4.0 mm triple resonance probes configured in HX double mode. The 2.5 mm rotors and 4.0 mm rotors were spun at frequencies of 25 kHz and 10 kHz respectively. On both probes ^{29}Si pulses calibrated on tetrakis(trimethylsilyl)silane (TMSS) and pulse durations and RF fields were assumed to be identical for ^{77}Se. MAS ^{77}Se SSNMR spectra were acquired with a rotor-synchronized CPMG pulse sequence[94] and rectangular excitation pulses. For the 2.5 mm probe the ^{77}Se π/2 and π pulse durations were 3.53 μs and 7.07 μs, respectively, with 75 W of input power. For the 4.0 mm probe the ^{77}Se π/2 and π pulse durations were 6.0 μs and 12.0 μs, respectively, with 100 W of input power. For CPMG experiments with a 25 kHz MAS frequency each echo cycle was 0.72 ms in duration (including signal acquisition for 0.64 ms, ring down delays and pulses). 2048 to 4096 spin echoes were acquired, except for WSe_2, for which 32 echoes were acquired. Additional direct excitation ^{77}Se CPMG MAS SSNMR experiments with sample temperatures of 110 K were performed on WSe_2 and $MoSe_2$ using a 3.2 mm MAS probe and the

DNP spectrometer described below. The MAS frequency was 10 kHz. The ^{77}Se $\pi/2$ and π pulse durations were 3.5 μs and 7.0 μs, respectively, with 120 W of input power. Recycle delays of 1000 s were used and 8 scans were acquired.

Dynamic nuclear polarization NMR. MAS DNP SSNMR experiments were performed with a commercial Bruker 400 MHz / 263 GHz (^{1}H /electron frequencies) DNP spectrometer equipped with a Bruker Avance III spectrometer.[95] The main magnetic field was set so that microwave irradiation occurred at the EPR frequency that gives maximum positive DNP enhancement with nitroxide biradicals. Experiments were performed with a 3.2 mm Bruker HXY probe configured in ^{1}H-^{77}Se double resonance HX mode. The sample temperature with microwaves was approximately 110 K. For sample preparation, between 40 mg and 75 mg of WSe_2 or $MoSe_2$ was impregnated with 10 μL of a 16 mM TEKPol 1,1,2,2-tetrachloroethane (TCE) solution.[96] Samples made with the incorrect ratio of solvent, either too much or too little, resulted in low or no DNP enhancement. The sample of amine intercalated WSe_2 nanocrystals was prepared by impregnating 10 mg of the nanocrystals with 5 μL of a 16 mM TEKPol TCE solution. This was not enough material to fill the 3.2 mm rotor. To address this problem the rotor was first packed with enough powdered NaCl to center the impregnated nanocrystals in the coil. The impregnated nanocrystals were then packed into the rotor and capped with an additional layer of NaCl, then capped with a polytetrafluoroethylene insert. The ^{1}H→^{77}Se CP conditions and ^{77}Se pulse durations were calibrated using DNP-enhanced ^{1}H→^{29}Si CPMAS experiments on TEKPol/TCE impregnated alkyl-functionalized silicon nanocrystals.[97] ^{1}H→^{77}Se CP/CPMG experiments used CP contact times of 7 ms. The CP contact pulses used approximate ^{1}H and ^{77}Se RF fields of 55 kHz and 50 kHz, respectively. The amplitude of the ^{1}H contact pulse was ramped from 90% to 100% intensity in order to broaden the CP match condition. The CPMG acquisition used echo

cycles 1.0 ms in duration and 32 to 40 spin echoes were acquired. The CP pulse-cooling pulse sequence[83,84] with CPMG detection was used to acquire DNP-enhanced ^{77}Se SSNMR spectra of WSe_2 and $MoSe_2$. The pulse-cooling experiments used 17 CP steps with delays of 3 seconds in between the CP steps. Each CP step used a contact time of 7 ms. The CPMG acquisition used echo cycles 1.2 ms in duration and 18 spin echoes were acquired. SPINAL-64 ^{1}H heteronuclear decoupling was applied during signal acquisition in all DNP experiments.[98] The ^{1}H RF field was 100 kHz for WSe_2 and $MoSe_2$ and was 70 kHz for the WSe_2 nanocrystals.

Planewave DFT Calculations. Periodic gauge-including projector augmented waves (GIPAW)[78] planewave DFT calculations were performed using the CASTEP[77] module as implemented in Materials Studio (Dassault Systemes). Calculations used unit cells and atomic coordinates from the standard crystal structures of $MoSe_2$ (ICSD#25391) and WSe_2 (ICSD (#40752). *k*-point spacing and energy cut-off tests were performed to confirm convergence of the calculated ^{77}Se shielding values of WSe_2. *k*-point spacings of less than 0.04 $Å^{-1}$ and cutoff values of 500 eV or higher gave converged shielding values. Chemical shift calculations were performed on both WSe_2 and $MoSe_2$. We also performed calculations where the atomic coordinates and unit cell were relaxed prior to the NMR calculations. Calculations on $Mo_{0.5}W_{0.5}Se_2$ were performed by making a $2a\times4b\times1c$ supercell of WSe_2. Half of the W atoms were then replaced with Mo as illustrated in Figure S12. The placement of the Mo atoms was chosen to give Se atoms having coordination environments ranging from $SeMo_3$ to SeW_3. The structure was fully geometry optimized prior to running NMR calculations.

ASSOCIATED CONTENT

Supporting Information. Additional PXRD patterns, composition analysis, changes in PXRD pattern with lattice parameter and Scherrer size in mixed $MoSe_2$ and WSe_2 TMDCs, SEM images and elemental mapping, additional ^{77}Se SSNMR data and CASTEP ouput files. Raw NMR data for main text figures is available at: https://zenodo.org/records/10932473 or DOI:10.5281/zenodo.10932472.

Corresponding Author Information

Aaron J. Rossini − US DOE Ames National Laboratory, Ames, Iowa 50011, United States; Department of Chemistry, Iowa State University, Ames, Iowa 50011, United States; orcid.org/0000-0002-1679-9203; Email: arossini@iastate.edu

Javier Vela − US DOE Ames National Laboratory, Ames, Iowa 50011, United States; Department of Chemistry, Iowa State University, Ames, Iowa 50011, United States; orcid.org/0000-0001-5124-6893; Email: vela@iastate.edu

Acknowledgements

This research is supported by the U.S. Department of Energy (DOE), Office of Science, Basic Energy Sciences, Materials Science and Engineering Division. The research was performed at Ames National Laboratory, which is operated for the U.S. DOE by Iowa State University under Contract No. DE-AC02-07CH11358. Synthesis and standard characterization of WSe_2 nanocrystals (H.Y., J.Q.G, and A.M.S) was supported by the National Science Foundation (CHE-2003675 to A.M.S.). We thank Dr. Yunhua Chen for valuable discussions.

References

[1] Kolobov, A. V.; Tominaga, J. *Two-Dimensional Transition-Metal Dichalcogenides*; Springer International Publishing AG: Switzerland, 2016.

[2] Iacopi, F.; Boeckl, J. J.; Jagadish, C. *2D Materials*. Academic Press: Cambridge, MA, 2016.

[3] Cai, Z.; Liu, B.; Zou, X.; Cheng, H.-M. Chemical Vapor Deposition Growth and Applications of Two-Dimensional Materials and Their Heterostructures. *Chem. Rev.* **2018**, *118* (13), 6091–6133.

[4] Coleman, J. N.; Lotya, M.; O'Neill, A.; Bergin, S. D.; King, P. J.; Khan, U.; Young, K.; Gaucher, A.; De, S.; Smith, R. J.; *et al.* Two-Dimensional Nanosheets Produced by Liquid Exfoliation of Layered Materials. *Science* **2011**, *331* (6017), 568–571.

[5] Susarla, S.; Hachtel, J. A.; Yang, X.; Kutana, A.; Apte, A.; Jin, Z.; Vajtai, R.; Idrobo, J. C.; Lou, J.; Yakobson, B. I.; Tiwary, C. S.; Ajayan, P. M. Thermally Induced 2D Alloy-Heterostructure Transformation in Quaternary Alloys. *Adv. Mater.* **2018**, *30* (45), 1804218.

[6] Geim, A.K.; Grigorieva, I.V., Van Der Waals Heterostructures. *Nature* **2013**, *499,* 419–425.

[7] Choi, W.; Choudhary, N.; Han, G. H.; Park, J.; Akinwade, D.; Lee, Y. H. Recent Development of Two-Dimensional Transition Metal Dichalgogenides and Their Applications. *Mater. Today* **2017**, *20* (3), 116–130.

[8] Thomazeau, C.; Geantet, C.; Lacroix, M.; Harlé, V.; Benazeth, S.; Marhic, C.; Danot, M. Two Cation Disulfide Layers in the $W_xMo_{(1-x)}S_2$ Lammelar Solid Solution. *J. Solid State Chem.* **2001**, *160*, 147–155.

[9] Hlova, I. Z.; Dolotko, O.; Boote, B. W.; Pathak, A. K.; Smith, E. A.; Pecharsky, V. K.; Balema, V. P. Multi-Principal Element Transition Metal Dichalcogenides via Reactive Fusion of 3D-Heterostructures. *Chem. Commun.* **2018**, *54* (89), 12574–12577.

[10] Silva, I. d. A. A.; Bartalucci, E.; Bolm, C.; Wiegand, T. Opportunities and Challenges in Applying Solid-State NMR Spectroscopy in Organic Mechanochemistry. *Adv. Mater.* **2023**, *35*, 2304092.

[11] Schiffmann, J. G.; Emmerling, F.; Martins, I. C. B.; Van Wüllen, L. In-Situ Reaction Monitoring of a Mechanochemical Ball Mill Reaction with Solid State NMR. *Solid State Nucl. Magn. Reson.* **2020**, *109*, 101687.

[12] Jakobsen, H.J.; Bildsøe, H.; Bondesgaard, M.; Iversen, B.B.; Brorson, M.; Larsen, F.H.; Gan, Z.; Hung, I. Exciting Opportunities for Solid-State ^{95}Mo NMR Studies of MoS_2 Nanostructures in Materials Research from a Low to an Ultrahigh Magnetic Field (35.2 T). *The J. Phys. Chem. C* **2021**, *125* (14), 7824–7838.

[13] Jakobsen, H.J.; Bildsøe, H.; Skibsted, J.; Brorson, M.; Schaumburg, K. Natural Abundance Solid-State ^{95}Mo MAS NMR of MoS_2 Reveals Precise ^{95}Mo Anisotropic Parameters from its Central and Satellite Transitions. *Chem. Commun.* **2010**, *46* (12), 2103–2105.

[14] O'Dell, L.A.; Moudrakovski, I.L. Testing the Sensitivity Limits of ^{33}S NMR: An Ultra-Wideline Study of Elemental Sulfur. *J. Magn. Reson.* **2010**, *207* (2), 345–347.

[15] Marple, M.; Badger, J.; Hung, I.; Gan, Z.; Kovnir, K.; Sen, S. Structure of Amorphous Selenium by 2D ^{77}Se NMR Spectroscopy: An End to the Dilemma of Chain versus Ring. *Angew. Chem. Int. Ed.*. **2017**, *56* (33), 9777–9781.

[16] Kemp, T. F.; Wong, A.; Smith, M. E.; Bishop, P. T.; Carthey, N. A Natural Abundance ^{77}Se Solid-State NMR Study of Inorganic Compounds. *Solid State Nucl. Magn. Reson.* **2008**, *34* (4), 224–227.

[17] Kaseman, D. C.; Hung, I.; Gan, Z.; Sen, S. Observation of a Continuous Random Network Structure in Ge_xSe_{100-x} Glasses: Results from High-Resolution ^{77}Se MATPASS/CPMG NMR Spectroscopy. *J. Phys. Chem. B* **2013**, *117* (3), 949–954.

[18] Griffin, J. M.; Knight, F. R.; Hua, G.; Ferrara, J. S.; Hogan, S. W.; Woollins, J. D.; Ashbrook, S. E. ^{77}Se Solid-State NMR of Inorganic and Organoselenium Systems: A Combined Experimental and Computational Study. *J. Phys. Chem. C* **2011**, *115* (21), 10859–10872.

[19] Demko, B. A.; Wasylishen, R. E. Solid-State Selenium-77 NMR. *Prog. Nucl. Magn. Reson. Spectrosc.* **2009**, *54* (3-4), 208–238.

[20] Chen, Y.; Dorn, R. W.; Hanrahan, M. P.; Wei, L.; Blome-Fernandez, R.; Medina-Gonzalez, A. M.; Adamson, M. A. S.; Flintgruber, A. H.; Vela, J.; Rossini, A. J. Revealing the Surface Structure of CdSe Nanocrystals by Dynamic Nuclear Polarization-Enhanced ^{77}Se and ^{113}Cd Solid-State NMR Spectroscopy. *J. Am. Chem. Soc.* **2021**, *143* (23), 8747–8760.

[21] Piveteau, L.; Ong, T. C.; Rossini, A. J.; Emsley, L.; Copéret, C.; Kovalenko, M. V. Structure of Colloidal Quantum Dots from Dynamic Nuclear Polarization Surface Enhanced NMR Spectroscopy. *J. Am. Chem. Soc.* **2015**, *137* (43), 13964–13971.

[22] Ratcliffe, C. I.; Yu, K.; Ripmeester, J. A.; Zaman, M. B.; Badarau, C.; Singh, S. Solid State NMR Studies of Photoluminescent Cadmium Chalcogenide Nanoparticles. *Phys. Chem. Chem. Phys.* **2006**, *8* (30), 3510–3519.

[23] Thayer, A. M.; Steigerwald, M. L.; Duncan, T. M.; Douglass, D. C. NMR Study of Semiconductor Molecular Clusters. *Phys. Rev. Lett.* **1988**, *60* (25), 2673–2676.

[24] Lovingood, D. D.; Achey, R.; Paravastu, A. K.; Strouse, G. F. Size- and Site-Dependent Reconstruction in CdSe QDs Evidenced by $^{77}Se\{^{1}H\}$ CP-MAS NMR Spectroscopy. *J. Am. Chem. Soc.* **2010**, *132* (10), 3344–3354.

[25] Berrettini, M. G.; Braun, G.; Hu, J. G.; Strouse, G. F. NMR Analysis of Surfaces and Interfaces in 2-nm CdSe. *J. Am. Chem. Soc.* **2004**, *126* (22), 7063–7070.

[26] Dupree, R.; Warren, W. W. J.; DiSalvo, F. J. J. ^{77}Se NMR Study of the Electronic Instability in $TiSe_2$. *Phys. Rev. B* **1977**, *16* (3), 1001–1007.

[27] Borsa, F.; Torgeson, D. R.; Shanks, H. R. Charge-Density Wave Amplitudes in 2H−$NbSe_2$ and 2H−$TaSe_2$ Determined by ^{77}Se NMR. *Phys. Rev. B* **1977**, *15* (10), 4576–4579.

[28]Dolotko, O.; Hlova, I. Z.; Pathak, A. K.; Mudryk, Y.; Pecharsky, V. K.; Singh, P.; Johnson, D. D.; Boote, B. W.; Li, J.; Smith, E. A.; *et al.* Unprecedented Generation of 3D Heterostructures by Mechanochemical Disassembly and Re-ordering of Incommensurate Metal Chalcogenides. *Nat. Commun.* **2020**, *11*, 1–10.

[29] Skripov, A.V.; Sibirtsev, D.S.; Cherepanov, Y.G.; Aleksashin, B.A. ^{77}Se NMR Study of the Charge Density Wave State in 2H-$NbSe_2$ and 1T-VSe_2. *J. Phys. Condens. Matter* **1995**, *7* (23), 4479–4487.

[30] Borsa, F.; Torgeson, D.R.; Shanks, H.R. Charge-Density Wave Amplitudes in 2H-$NbSe_2$ and 2H-$TaSe_2$ Determined by ^{77}Se NMR. *Phys. Rev. B* **1977**, *15* (10), 4576–4579.

[31] Dupree, R.; Warren Jr, W.W.; DiSalvo Jr, F.J. ^{77}Se NMR Study of the Electronic Instability in $TiSe_2$. *Phys. Rev. B* **1977**, *16* (3), 1001–1007.

[32] Gi, E.; Chen, Y.; Wang, X. R.; Carnahan, S. L.; Rahman, S.; Smith, E. A.; Rossini, A. J.; Vela, J. Chemical-Induced Slippage in Bulk WSe_2. *J. Phys. Chem. Lett.* **2022**, *13*, 10924–10928.

[33] Ni, Q.Z.; Daviso, E.; Can, T.V.; Markhasin, E.; Jawla, S.K.; Swager, T.M.; Temkin, R.J.; Herzfeld, J.; Griffin, R.G. High Frequency Dynamic Nuclear Polarization. *Acc. Chem. Res.* **2013**, *46* (9), 1933–1941.

[34] Maly, T.; Debelouchina, G.T.; Bajaj, V.S.; Hu, K.N.; Joo, C.G.; Mak–Jurkauskas, M.L.; Sirigiri, J.R.; Van Der Wel, P.C.; Herzfeld, J.; Temkin, R.J.; *et al.* Dynamic Nuclear Polarization at High Magnetic Fields. *J. Chem. Phys.* **2008**, *128* (5), 052211.

[35] Rossini, A.J.; Zagdoun, A.; Lelli, M.; Lesage, A.; Copéret, C.; Emsley, L. Dynamic Nuclear Polarization Surface Enhanced NMR Spectroscopy. *Acc. Chem. Res.* **2013**, *46* (9), 1942–1951.

[36] Lim, D.J.; Marks, N.A.; Rowles, M.R. Universal Scherrer Equation for Graphene Fragments. *Carbon* **2020**, *162*, 475-480.

[37] Holder, C. F.; Schaak, R. E. Tutorial on Powder X-Ray Diffraction for Characterizing Nanoscale Materials. *ACS Nano* **2019**, *13* (7), 7359–7365.

[38] Miranda, M.A.R.; Sasaki, J.M. The Limit of Application of the Scherrer Equation. *Acta Cryst. A* **2018**, *74* (1), 54–65.

[39] Suryanarayana, C. Mechanical Alloying and Milling. *Prog. Mater. Sci.* **2001**, *46* (1-2), 1–184.

[40]Xie, J., Zhang, H.; Li, S.; Wang, R.; Sun, X.; Zhou, M.; Zhou, J.; Lou, X.W.; Xie, Y.; Defect-rich MoS_2 Ultrathin Nanosheets with Additional Active Edge Sites for Enhanced Electrocatalytic Hydrogen Evolution. *Adv. Mater.* **2013**, *25* (40), 5807-5813.

[41] Si, K.; Ma, J.; Lu, C.; Zhou, Y.; He, C.; Yang, D.; Wang, X.; Xu, X. A Two-Dimensional Mos_2/WSe_2 Van der Waals Heterostructure for Enhanced Photoelectric Performance. *Appl. Surf. Sci.* **2020**, *507*, 145082.

[42] Kuo, D. Y.; Cossairt, B. M. Direct Intercalation of MoS_2 and WS_2 Thin Films by Vacuum Filtration. *Mater. Horiz.* **2022**, *9*, 360−367.

[43] Hlova, I. Z.; Singh, P.; Malynych, S. Z.; Gamernyk, R. V.; Dolotko, O.; Pecharsky, V. K.; Johnson, D. D.; Arroyave, R.; Pathak, A. K.; Balema, V. P. Incommensurate Transition-Metal Dichalcogenides *via* Mechanochemical Reshuffling of Binary Precursors. *Nanoscale Adv.* **2021**, *3* (14), 4065–4071.

[44] Yang, L.; Cui, X.; Zhang, J.; Wang, K.; Shen, M.; Zeng, S.; Dayeh, S.A.; Feng, L.; Xiang, B. Lattice Strain Effects on the Optical Properties of Mos_2 Nanosheets. *Sci. Rep.* **2014**, *4* (1), 5649.

[45] Kiran, V.; Mukherjee, D.; Jenjeti, R.N.; Sampath, S. Active Guests in the $Mos_2/Mose_2$ Host Lattice: Efficient Hydrogen Evolution Using Few-Layer Alloys of $Mos_{2(1-X)}Se_{2x}$. *Nanoscale* **2014**, *6* (21), 12856–12863.

[46] El-Eskandarany, M.S. *Mechanical Alloying: Nanotechnology, Materials Science and Powder Metallurgy*, 2nd ed.; Elsevier: Oxford, UK, 2015.

[47] Rosales, B.A.; Wei, L.; Vela, J. Synthesis and Mixing of Complex Halide Perovskites by Solvent-Free Solid-State Methods. *J. Solid State Chem.* **2019**, *271*, 206–215.

[48] Reichert, M.D.; Lin, C.C.; Vela, J. How Robust Are Semiconductor Nanorods? Investigating the Stability and Chemical Decomposition Pathways of Photoactive Nanocrystals. *Chem. Mater*. **2014**, *26* (13), 3900–3908.

[49] Zhong, H.; Quhe, R.; Wang, Y.; Ni, Z.; Ye, M.; Song, Z.; Pan, Y.; Yang, J.; Yang, L.; Lei, M.; Shi, J.; Lu, J. Interfacial Properties of Monolayer and Bilayer MoS2 Contacts with Metals: Beyond the Energy Band Calculations. *Sci. Rep.* **2016**, *6* (1), 21786.

[50] Gusakova, J.; Wang, X.; Shiau, L.L.; Krivosheeva, A.; Shaposhnikov, V.; Borisenko, V.; Gusakov, V.; Tay, B.K. Electronic Properties of Bulk and Monolayer TMDs: Theoretical Study within DFT Framework (GVJ-2e Method). *Phys. Status Solidi (a)*, **2017**, *214*(12), 1700218.

[51] Kuc, A.; Zibouche, N.; Heine, T. Influence of Quantum Confinement on the Electronic Structure of the Transition Metal Sulfide TS_2. *Phys. Rev. B*, **2011**, *83*(24), 245213.

[52] Kam, K.K.; Parkinson, B.A. Detailed Photocurrent Spectroscopy of the Semiconducting Group VIB Transition Metal Dichalcogenides. *J. Phys. Chem.* **1982**, *86*(4), 463–467.

[53] Liu, H.L.; Shen, C.C.; Su, S.H.; Hsu, C.L.; Li, M.Y.; Li, L.J. Optical Properties of Monolayer Transition Metal Dichalcogenides Probed by Spectroscopic Ellipsometry. *Appl. Phys. Lett.* **2014**, *105*(20), 201905.

[54] Niu, Y.; Gonzalez-Abad, S.; Frisenda, R.; Marauhn, P.; Drüppel, M.; Gant, P.; Schmidt, R.; Taghavi, N.S.; Barcons, D.; Molina-Mendoza, A.J.; *et al.* Thickness-Dependent Differential Reflectance Spectra of Monolayer and Few-Layer MoS_2, $MoSe_2$, WS_2 and WSe_2. *Nanomaterials*, **2018**, *8*(9), 725.

[55] Liu, B.; Abbas, A.; Zhou, C. Two-Dimensional Semiconductors: From Materials Preparation to Electronic Applications. *Adv. Electron. Mater.* **2017**, *3* (7), 1700045.

[56] Thripuranthaka, M.; Kashid, R. V.; Sekhar Rout, C.; Late, D. J. Temperature Dependent Raman Spectroscopy of Chemically Derived Few Layer MoS_2 and WS_2 Nanosheets. *Appl. Phys. Lett.* **2014**, *104* (8), 081911.

[57] Kumar, R.; Jenjeti, R. N.; Vankayala, K.; Sampath, S. Quaternary, Layered, 2D Chalcogenide, $Mo_{1-x}W_xSSe$: Thickness Dependent Transport Properties. *Nanotechnol.* **2024**, *35* (4), 045202.

[58] Dumcenco, D. O.; Chen, K. Y.; Wang, Y. P.; Huang, Y. S.; Tiong, K. K. Raman Study of 2H-$Mo_{1-x}W_xS_2$ Layered Mixed Crystals. *J. Alloys Compd.* **2010**, *506* (2), 940–943.

[59] Jenjeti, R. N.; Kumar, R.; Vankayala, K.; Sampath, S. Optothermal and Electrical Properties of Ultrathin Alloys of Mixed Dichalcogenides. *J. Mater. Sci.* **2022**, *57* (30), 14339–14355.

[60] Kuhnert, J.; Rahimi-Iman, A.; Heimbrodt, W. Magneto Photoluminescence Measurements of Tungsten Disulphide Monolayers. *J. Phys.: Condens. Matter* **2017**, *29* (8), 08LT02.

[61] Zhao, W.; Ghorannevis, Z.; Amara, K. K.; Pang, J. R.; Toh, M.; Zhang, X.; Kloc, C.; Tan, P. H.; Eda, G. Lattice Dynamics in Mono- and Few-Layer Sheets of WS_2 and WSe_2. *Nanoscale* **2013**, *5* (20), 9677.

[62] Pines, A.; Gibby, M. G.; Waugh, J. S. Proton-Enhanced NMR of Dilute Spins in Solids. *J. Chem. Phys.* **1973**, *59* (2), 569–590.

[63] Wei, D.; Han, M.; Yu, L. Solid-State ^{77}Se NMR of Organoselenium Compounds through Cross Polarization Magic Angle Spinning (CPMAS) Method. *Sci. Rep.* **2017**, *7* (1), 6376.

[64] Rossini, A. J., Materials Characterization by Dynamic Nuclear Polarization-Enhanced Solid-State NMR Spectroscopy. *J. Phys. Chem. Lett.* **2018**, *9* (17), 5150–5159.

[65] Thankamony, A. S. L.; Wittmann, J. J.; Kaushik, M.; Corzilius, B., Dynamic Nuclear Polarization for Sensitivity Enhancement in Modern Solid-State NMR. *Prog. Nucl. Magn. Reson. Spectrosc.* **2017**, *102-103*, 120–195.

[66] Ni, Q. Z.; Daviso, E.; Can, T. V.; Markhasin, E.; Jawla, S. K.; Swager, T. M.; Temkin, R. J.; Herzfeld, J.; Griffin, R. G., High Frequency Dynamic Nuclear Polarization. *Acc. Chem. Res.* **2013**, *46* (9), 1933–1941.

[67] Rossini, A. J.; Zagdoun, A.; Lelli, M.; Lesage, A.; Coperet, C.; Emsley, L., Dynamic Nuclear Polarization Surface Enhanced NMR Spectroscopy. *Acc. Chem. Res.* **2013**, *46* (9), 1942–1951.

[68] O'Dell, L.A. and Schurko, R.W., QCPMG Using Adiabatic Pulses for Faster Acquisition of Ultra-Wideline NMR Spectra. *Chem. Phys. Lett.* **2008**, *464* (1-3), 97–102.

[69] O'Dell, L. A. The WURST Kind of Pulses in Solid-State NMR. *Solid State Nucl. Magn. Reson.* **2013**, *55-56*, 28–41.

[70] Meiboom, S.; Gill, D. Modified Spin-Echo Method for Measuring Nuclear Relaxation Times. *Rev. Sci. Instrum.* **1958**, *29* (8), 688–691.

[71] Carr, H. Y.; Purcell, E. M. Effects of Diffusion on Free Precession in Nuclear Magnetic Resonance Experiments. *Phys. Rev.* **1954**, *94* (3), 630–638.

[72] O'Dell, L.A.; Rossini, A.J.; Schurko, R.W. Acquisition of Ultra-Wideline NMR Spectra from Quadrupolar Nuclei by Frequency Stepped WURST–QCPMG. *Chem. Phys. Lett.* **2009**, *468* (4-6), 330–335.

[73] Murray, R.; Evans, B. The Thermal Expansion of 2H-MoS_2 and 2H-WSe_2 between 10 and 320 K. *J. Appl. Cryst.* **1979**, *12*(3), 312–315.

[74] Tanabe, I.; Komesu, T.; Le, D.; Rawal, T.B.; Schwier, E.F.; Zheng, M.; Kojima, Y.; Iwasawa, H.; Shimada, K.; Rahman, T.S.; *et al.* The Symmetry-Resolved Electronic Structure of 2H-WSe_2 (0 0 0 1). *J. Phys. Condens. Matter* **2016**, *28*(34), 345503.

[75] Ashbrook, S. E.; McKay, D. Combining Solid-State NMR Spectroscopy with First-Principles Calculations - A Guide to NMR Crystallography. *Chem. Commun.* **2016**, *52* (45), 7186–7204.

[76] Yates, J. R.; Pickard, C. J.; Mauri, F. Calculation of NMR Chemical Shifts for Extended Systems Using Ultrasoft Pseudopotentials. *Phys. Rev. B* **2007**, *76* (2), 024401.

[77] Clark, S. J.; Segall, M. D.; Pickard, C. J.; Hasnip, P. J.; Probert, M. J.; Refson, K.; Payne, M. C., First Principles Methods Using CASTEP. *Z. Kristallogr.* **2005**, *220* (5-6), 567–570.

[78] Pickard, C. J.; Mauri, F. All-Electron Magnetic Response with Pseudopotentials: NMR Chemical Shifts. *Phys. Rev. B* **2001**, *63* (24), 245101.

[79] Lesage, A., Surface Enhanced NMR Spectroscopy by Dynamic Nuclear Polarization. *J. Am. Chem. Soc.* **2010**, *132*, 15459–15461.

[80] Zagdoun, A.; Casano, G.; Ouari, O.; Schwarzwälder, M.; Rossini, A. J.; Aussenac, F.; Yulikov, M.; Jeschke, G.; Copéret, C.; Lesage, A.; *et al.* Large Molecular Weight Nitroxide Biradicals Providing Efficient Dynamic Nuclear Polarization at Temperatures up to 200 K. *J. Am. Chem. Soc.* **2013**, *135* (34), 12790–12797.

[81] Zagdoun, A.; Rossini, A. J.; Gajan, D.; Bourdolle, A.; Ouari, O.; Rosay, M.; Maas, W. E.; Tordo, P.; Lelli, M.; Emsley, L.; Lesage, A.; Copéret, C. Non-Aqueous Solvents for DNP Surface Enhanced NMR Spectroscopy. *Chem. Commun.* **2012**, *48* (5), 654–656.

[82] Björgvinsdóttir, S.; Moutzouri, P.; Berruyer, P.; Hope, M. A.; Emsley, L. Sensitivity Enhancements in Lithium Titanates by Incipient Wetness Impregnation DNP NMR. *J. Phys. Chem. C* **2020**, *124* (30), 16524–16528.

[83] Bjorgvinsdottir, S.; Walder, B. J.; Matthey, N.; Emsley, L. Maximizing Nuclear Hyperpolarization in Pulse Cooling under MAS. *J. Magn. Reson.* **2019**, *300*, 142–148.

[84] Bjorgvinsdottir, S.; Walder, B. J.; Pinon, A. C.; Emsley, L. Bulk Nuclear Hyperpolarization of Inorganic Solids by Relay from the Surface. *J. Am. Chem. Soc.* **2018**, *140* (25), 7946–7951.

[85] Carnahan S.L., Riemersma K.T., Hlova I., Dolotko O., Kmiec S.J., Lamahewage S.N.S., Martin S.W., Wishart J.F., Dubroca T., Balema V.P., Rossini A.J. Formation of Stable Radicals by Mechanochemistry and Their Application for Magic Angle Spinning Dynamic Nuclear Polarization Solid-State NMR Spectroscopy. *J. Phys. Chem. A* **2024**, *128*, 3635–3645.

[86] Geisenhoff, J.Q.; Tamura, A.K; and Schimpf, A.M. Manipulation of Precursor Reactivity for the Facile Synthesis of Heterostructured and Hollow Metal Selenide Nanocrystals. *Chem. Mater.* **2020**, *32* (6), 2304–2312.

[87] Visser, J. W.; De Wolff, P. M. Absolute Intensities. Report 641.109, 1964, Technisch Physische Dienst, Delft, Netherlands.

[88] Match! - Phase Analysis using Powder Diffraction, Version 3.x, Crystal Impact - H. Putz & Dr. K. Brandenburg GbR, Kreuzherrenstr. 102, 53227 Bonn, Germany, https://www.crystalimpact.de/match.

[89] OriginPro, *Version 2024* OriginLab Corporation, Northampton, MA, USA

[90] Rodríguez-Carvajal, J. Recent Developments of the Program FULLPROF, in Commission on Powder Diffraction (IUCr). *Newslett.* **2001**, *26*, 12–19.

[91] Goldstein, J. I.; Newbury, D. E.; Echlin, P.; Joy, D. C.; Lyman, C. E.; Lifshin, E.; Sawyer, L.; Michael, J. R. *Scanning Electron Microscopy and X-Ray Microanalysis:* 3rd Ed.; Springer US: Boston, MA, 2003.

[92] Viezbicke, B. D.; Patel, S.; Davis, B. E.; Birnie, D. P. Evaluation of the Tauc Method for Optical Absorption Edge Determination: ZnO Thin Films as a Model System. *Phys. Status Solidi B* **2015**, *252*, 1700−1710.

[93] Klein, J.; Kampermann, L.; Mockenhaupt, B.; Behrens, M.; Strunk, J.; Bacher, G. Limitations of the Tauc Plot Method. *Adv. Funct. Mater.* **2023**, *33*(47), 2304523.

[94] Larsen, F. H.; Jakobsen, H. J.; Ellis, P. D.; Nielsen, N. Chr. High-Field QCPMG-MAS NMR of Half-Integer Quadrupolar Nuclei with Large Quadrupole Couplings. *Mol. Phys.* **1998**, *95* (6), 1185–1195.

[95] Rosay, M.; Tometich, L.; Pawsey, S.; Bader, R.; Schauwecker, R.; Blank, M.; Borchard, P. M.; Cauffman, S. R.; Felch, K. L.; Weber, R. T.; *et al.* Solid-State Dynamic Nuclear Polarization at 263 GHz: Spectrometer Design and Experimental Results. *Phys. Chem. Chem. Phys.* **2010**, *12* (22), 5850–5860.

[96] Zagdoun, A.; Casano, G.; Ouari, O.; Schwarzwälder, M.; Rossini, A. J.; Aussenac, F.; M., Y.; G., J.; Copéret, C.; Lesage, A.; Tordo, P.; Emsley, L. Large Molecular Weight Nitroxide Biradicals Providing Efficient Dynamic Nuclear Polarization at Temperatures up to 200 K. J. Am. Chem. Soc. 2013, 135, 12790-12797,

[97] Hanrahan, M. P.; Chen, Y.; Blome-Fernández, R.; Stein, J. L.; Pach, G. F.; Adamson, M. A. S.; Neale, N. R.; Cossairt, B. M.; Vela, J.; Rossini, A. J. Probing the Surface Structure of Semiconductor Nanoparticles by DNP SENS with Dielectric Support Materials. *J. Am. Chem. Soc.* **2019**, *141* (39), 15532–15546.

[98] Fung, B. M.; Khitrin, A. K.; Ermolaev, K. An Improved Broadband Decoupling Sequence for Liquid Crystals and Solids. *J. Magn. Reson.* **2000**, *142* (1), 97–101.

Supporting Information for:

Structural Studies of Alloyed and Nanoparticle Transition Metal Dichalcogenides by Selenium-77 Solid-State Nuclear Magnetic Resonance Spectroscopy

Scott L. Carnahan,[1,2,3‡] Eunbyeol Gi,[1,2,‡] Molly Wagner,[1,‡] Anuluxan Santhiran,[1,2] Elise Amerongen,[1,3] Hang Yin,[4] Jessica Q. Geisenhoff,[4] Sharifur Rahman,[1,2] Oleksandr Dolotko,[1] Ihor Hlova,[1] Viktor P. Balema,[1,5] Emily A. Smith,[1,2] Alina M. Schimpf,[4,6] Javier Vela,*[,1,2] and Aaron J. Rossini*[,1,2]

[1]US DOE Ames National Laboratory, Ames, Iowa, USA, 50011

[2]Iowa State University, Department of Chemistry, Ames, IA, USA, 50011

[3]Department of Chemistry, St. Mary's University of Minnesota, Winona, MN, USA, 55987

[4] Department of Chemistry and Biochemistry, University of California, San Diego, La Jolla, CA, USA, 92093

[5]Department of Materials Science & Engineering, Clemson University, Clemson, SC, USA, 29634

[6]Program in Materials Science and Engineering, University of California, San Diego, La Jolla, CA, USA, 92093

[‡]Equal contribution authors.

*Authors to Whom Correspondence Should be Addressed:

Professor Aaron J. Rossini – arossini@iastate.edu

Professor Javier Vela – vela@iastate.edu

Table of Contents for Supporting Information.

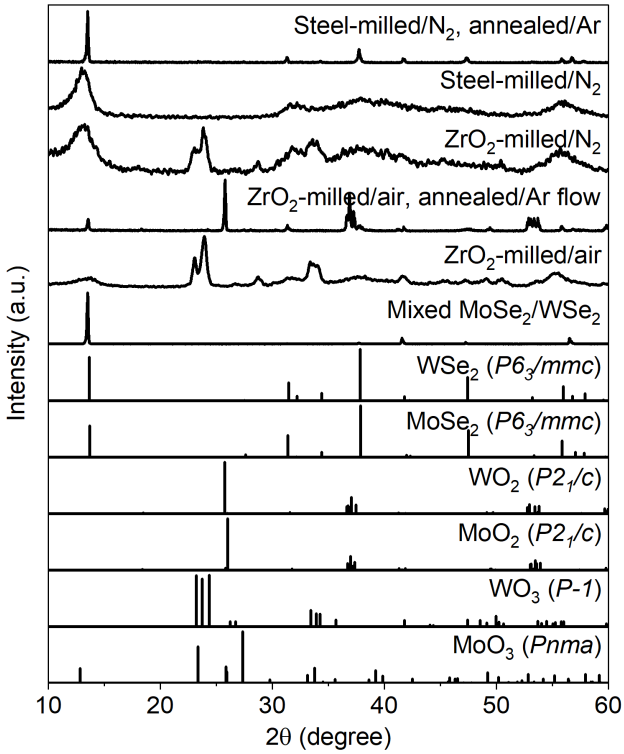

Figure S1. PXRD patterns of mixed TMDCs prepared under different conditions. Standard patterns of MoO_3 (#151750), WO_3 (#36168), MoO_2 (#23722), WO_2 (#80829), $MoSe_2$ (#25391), and WSe_2 (#40752) were adapted from Inorganic Crystal Structure Database (ICSD).

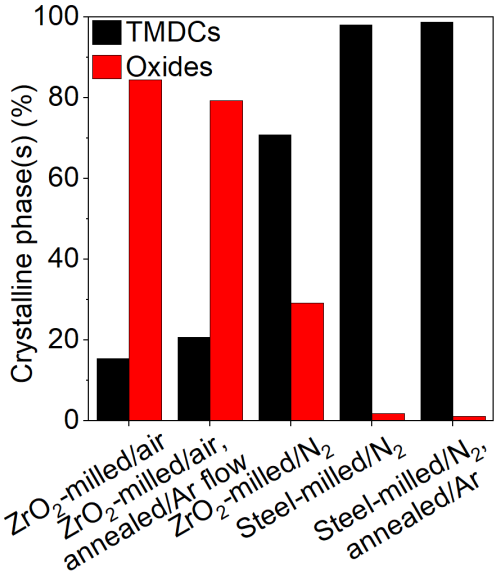

Figure S2. TMDCs *vs.* oxide(s) crystalline fraction of mixed TMDCs prepared under different conditions as estimated from fitting of PXRD patterns.

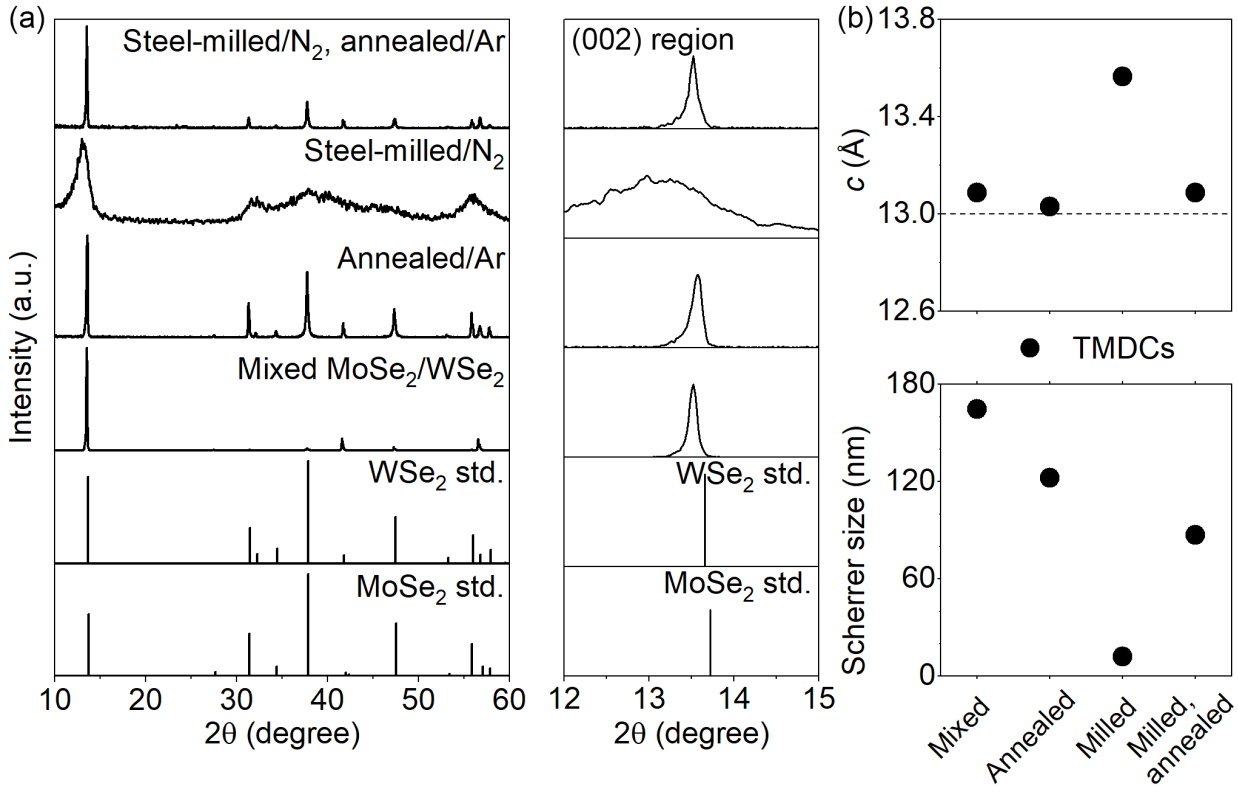

Figure S3. Changes in (a) PXRD patterns and (b) *c* lattice parameter and apparent Scherrer size as a function of mixing and alloying $MoSe_2$ with WSe_2 under different conditions. (Standard patterns of TMDC phases ($MoSe_2$-ICSD#25391, WSe_2-ICSD#40752) and (002) region shown for comparison in (a))

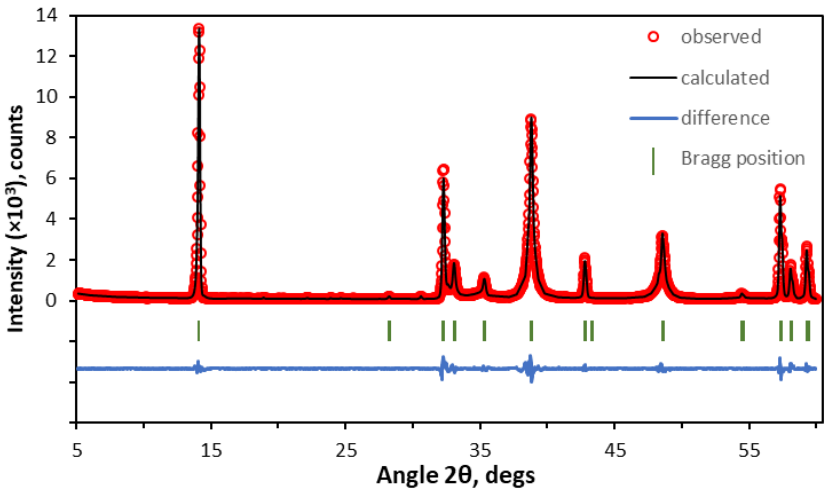

Figure S4. Rietveld refinement of the structure model based on XRD data of milled and annealed MoS_2 + WSe_2. Vertical bars at the bottom of the chart mark the calculated positions of Bragg peaks of the refined phase. The material crystallizes in space group $P6_3/mmc$, common for layered TMDCs, where Mo and W atoms randomly occupy the 2*c* position (1/3, 2/3, 1/4) in the crystal lattice. The 4*f* site (1/3, 2/3, *z*) is filled randomly with S and Se.

Table S1. Lattice parameters of mixed TMDCs.

TMDCs	*a* (Å)	*c* (Å)	Chalcogen *z*/c	R_p[b]
MoS_2	3.1601(2)	12.2886(5)	0.6170(2)	7.65
$MoSe_2$	3.2905(2)	12.9341(7)	0.6190(2)	8.64
WSe_2	3.2842(2)	12.9860(9)	0.6189(4)	7.72
Annealed MoS_2 + WSe_2	3.161(6)	12.378(1)	-	-
	3.265(2)	13.011(1)	-	-
Milled MoS_2 + WSe_2	-[a]	13.254(8)	-	-
Milled and annealed MoS_2 + WSe_2	3.2232(3)	12.7355(15)	0.6174(3)	6.09

[a]Some of the PXRD reflections of the milled samples were too broad, preventing an accurate determination of *a*.
[b]Column labelled R_p lists profile residuals.

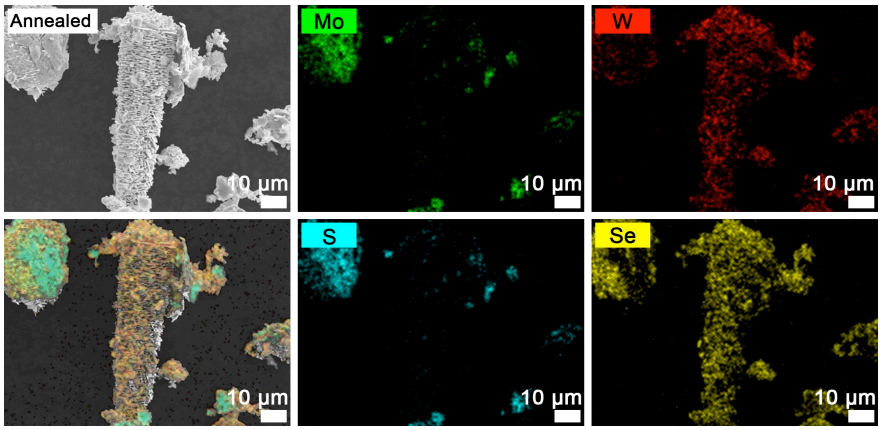

Figure S5. Representative SEM and EDS elemental mapping images of a directly annealed mixture of MoS_2 and WSe_2.

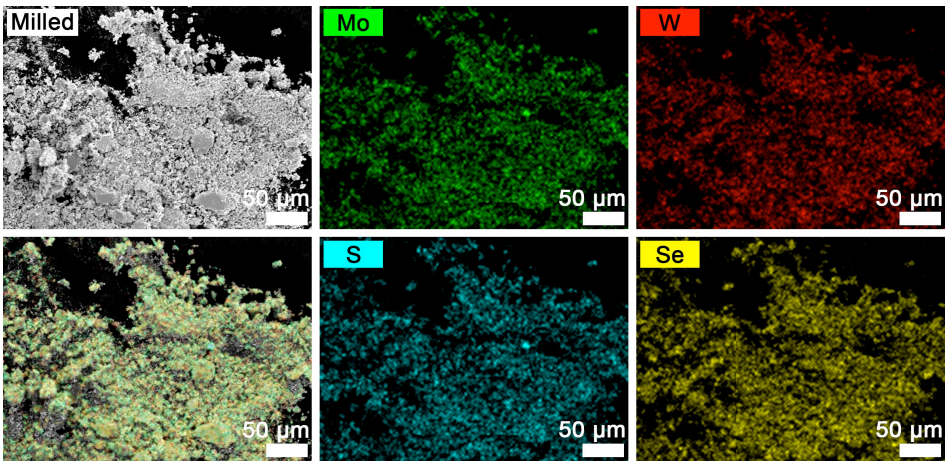

Figure S6. Representative SEM and EDS elemental mapping images of a milled mixture of MoS_2 and WSe_2.

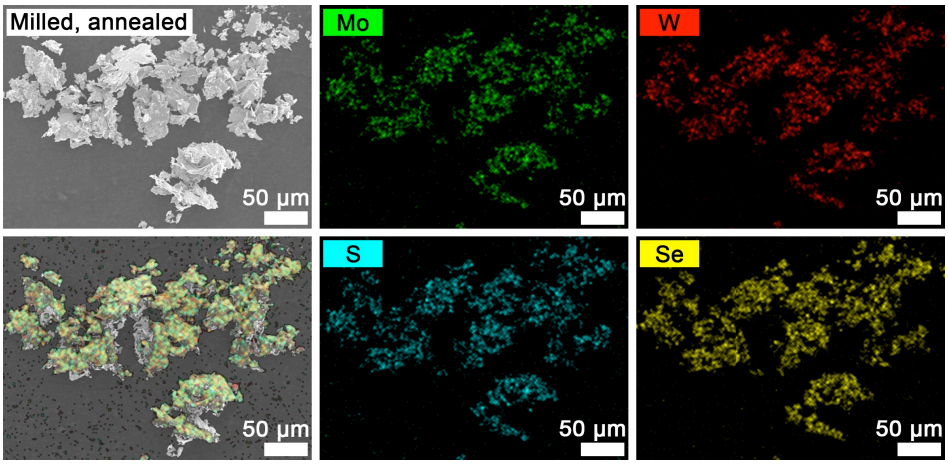

Figure S7. Representative SEM and EDS elemental mapping images of a milled and annealed mixture of MoS_2 and WSe_2.

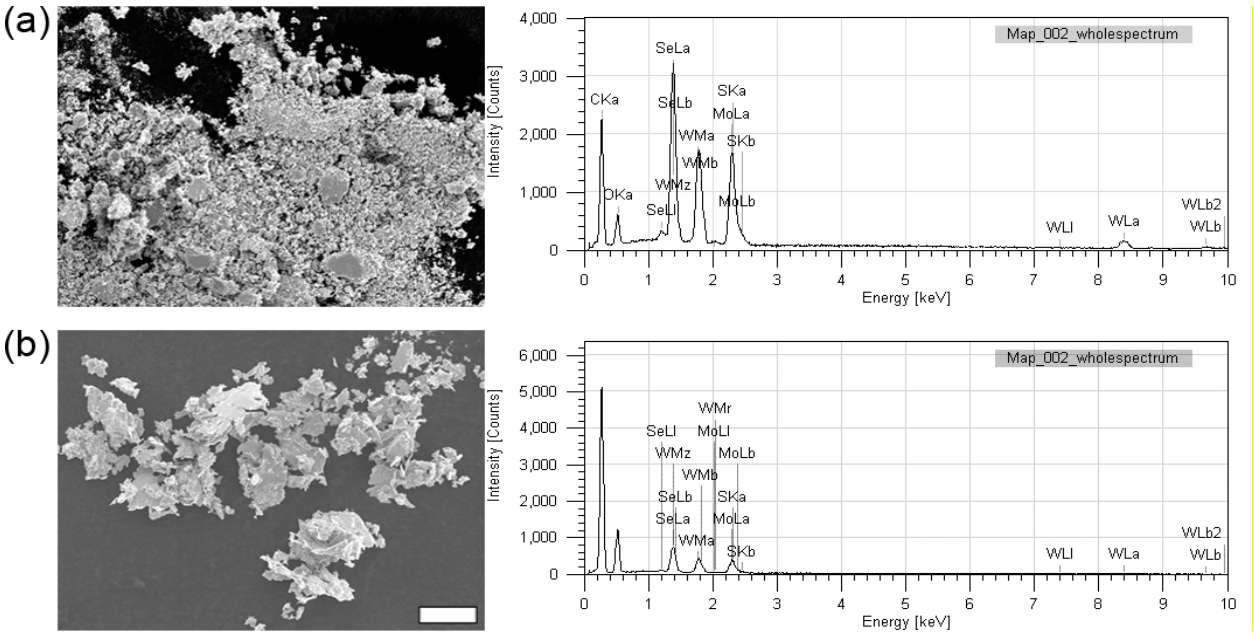

Figure S8. Representative SEM-EDX analysis of (a) milled and (b) milled and annealed mixture of MoS_2 and WSe_2.

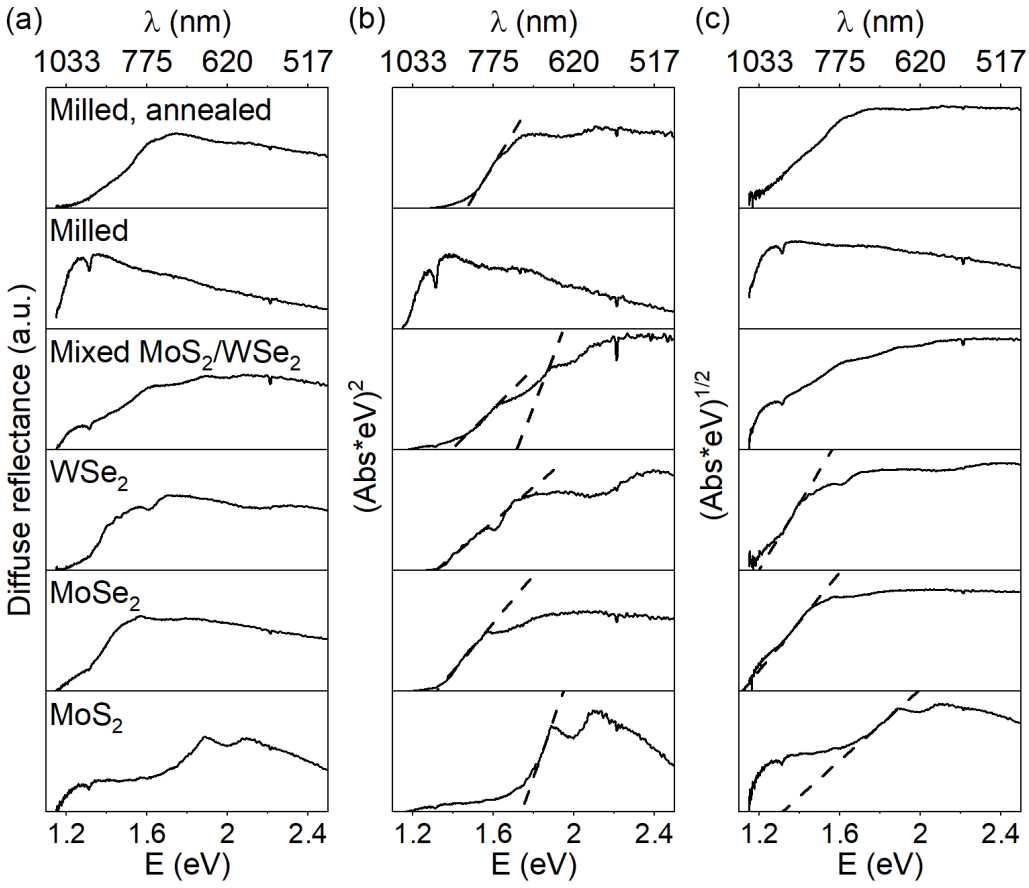

Figure S9. (a) Diffuse reflectance spectra, and corresponding (b) direct and (c) indirect Tauc plots as a function of mixing and alloying MoS_2 with WSe_2 under different conditions.

Table S2. Optical properties of TMDC materials.

		Band gaps		
		Measured, in eV (nm)[b]	Literature (calc.) in eV	
Precursor(s)	Experimental conditions[a]	Indirect (bulk[c])	Direct (1L[c])	Indirect (bulk[d])
MoS_2	None (as received)	1.3 (945)	1.9[S1] (1.7)[S2]	1.23[S3] (1.2)[S4]
$MoSe_2$	None (as received)	1.1 (1,115)	1.5[S1] (1.5)[S2]	1.1[S3] (1.1)[S5]
WSe_2	None (as received)	1.2 (1,030)	1.6[S1] (1.5)[S2]	1.2[S3] (1.2)[S6]
MoS_2+WSe_2	None (physical mix.)[a]	1.0 (1,290)	-	-
MoS_2+WSe_2	Ball-mill. (Steel/N_2, 24 h)	-	-	-
MoS_2+WSe_2	Ball-mill. (Steel/N_2, 24 h), anld. (1000 °C/Ar, 16 h)	1.1 (1,115)	-	-

[a]Samples prepared from multiple TMDCs were first physically-mixed at room temperature (RT = 21 °C) under air. [b]Diffuse reflectance (see Methods). [c]Monolayer (1L) to very-few-layers TMDCs. [d]Bulk TMDCs.

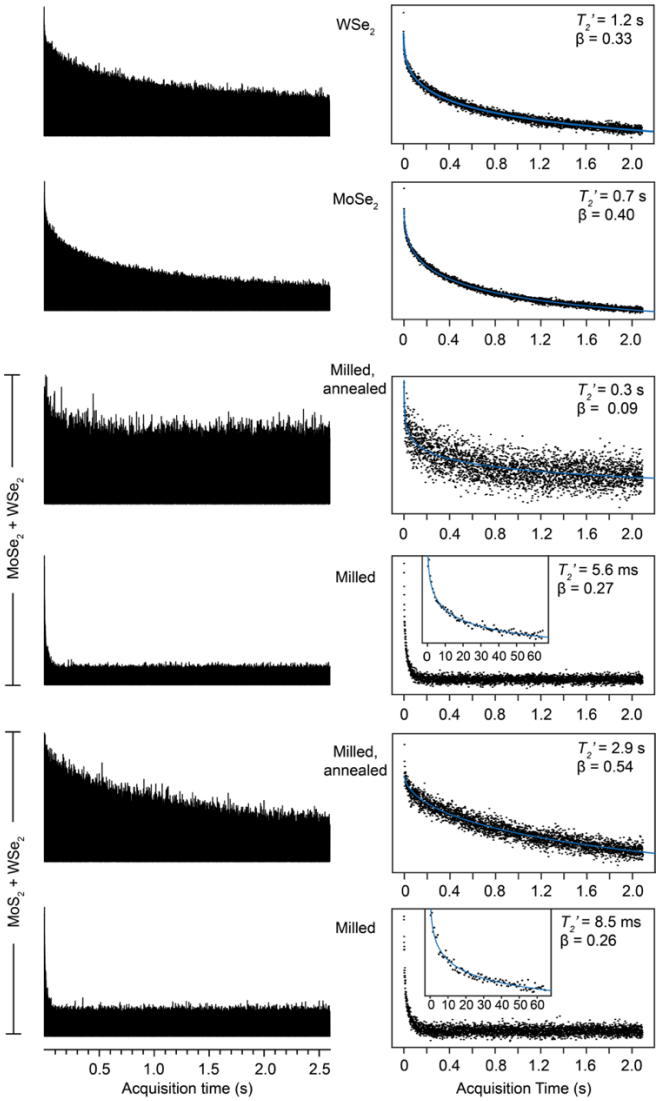

Figure S10. Measurements of the ^{77}Se T_2' from the decay of the WURST CPMG echo train for the indicated materials. Magnitude processed WURST CPMG echo trains are shown on the left. The right shows fits of the echo amplitudes to stretched exponential functions: $Signal\ Intensity = \exp\left(-\left(\frac{t}{T_2'}\right)^{\beta}\right)$, where t is the time value for each echo, T_2' is the fitted transverse relaxation time constant and b is the stretching exponent. The fitted values of T_2' and b are indicated on the plots.

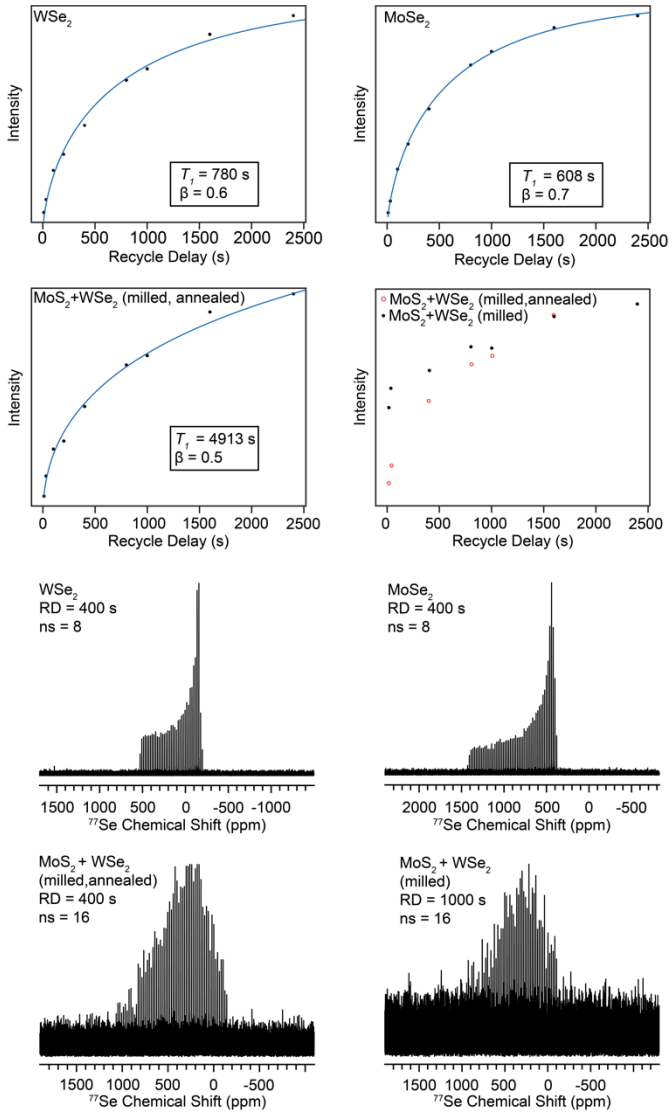

Figure S11. Results of ^{77}Se saturation recovery WURST CPMG experiments performed on WSe_2, $MoSe_2$, milled and annealed MoS_2 + WSe_2, and milled MoS_2 + WSe_2. The signal intensity is plotted as a function of the recycle delay. T_1 values were extracted by fitting the signal intensities with stretched exponential functions: $Signal\ Intensity = 1 - exp\left(1 - \left(\frac{t}{T_1}\right)^{\beta}\right)$, where t is the recycle delay, T_1 is the fitted longitudinal relaxation time constant and b is the stretching exponent. Fits with mono-exponential functions (b = 1.00) were unsatisfactory in all cases. For milled MoS_2 + WSe_2 we could not obtain satisfactory fits of the saturation curve due to a lack of data points at shorter recycle delays. Therefore, we compared the normalized saturation recovery curves for milled MoS_2 + WSe_2 to the curve for milled and annealed MoS_2 + WSe_2 to illustrate the faster signal build-up in the former. Static ^{77}Se SSNMR spectra obtained with 5.0 mm glass tubes (4.8 mm inner diameter) are shown below. The number of scans and recycle delay are indicated. Due to the larger sample volume offered by the glass tubes high quality ^{77}Se NMR spectra could be obtained with acquisition of only 8 or 16 scans.

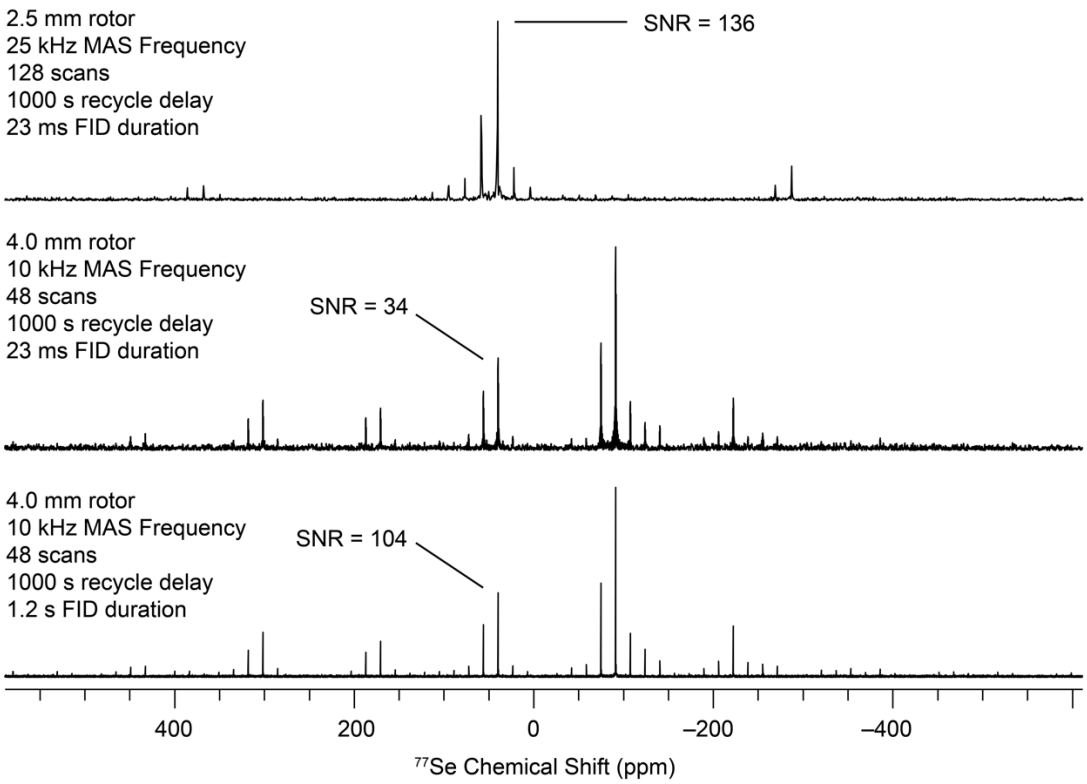

Figure S12. Comparison of MAS ^{77}Se SSNMR spectra of WSe_2 obtained with (upper) a 2.5 mm rotor and a 25 kHz MAS frequency or (lower two traces) a 4.0 mm rotor and a 10 kHz MAS frequency. The signal-to-noise ratio (SNR) for the isotropic peak and the number of scans acquired is indicated. All NMR spectra were acquired with a 1000 s recycle delay. The spectrum acquired with a 2.5 mm rotor used a total acquisition time of 23 ms, corresponding to acquisition of 32 spin echoes in the CPMG echo train. The spectrum acquired with the 4.0 mm rotor used a total acquisition time of 1.2 s, corresponding to acquisition of 1500 spin echoes in the CPMG echo train. In order to compare the SNR between the two different rotors, the FID of the 4.0 mm rotor was truncated to match the acquisition time of 23 ms used for experiments with the 2.5 mm rotor. For the middle spectrum only the first 29 spin echoes in the CPMG echo train were used in the Fourier Transform. After accounting for differences in the number of scans the 2.5 mm probe provides about 2.5 times better sensitivity per scan. Comparing spectra obtained with the same numbers of spin echoes shows that the 2.5 mm probe offers better sensitivity for the isotropic peak due to the reduction in sideband intensity and increase in the isotropic peak intensity.

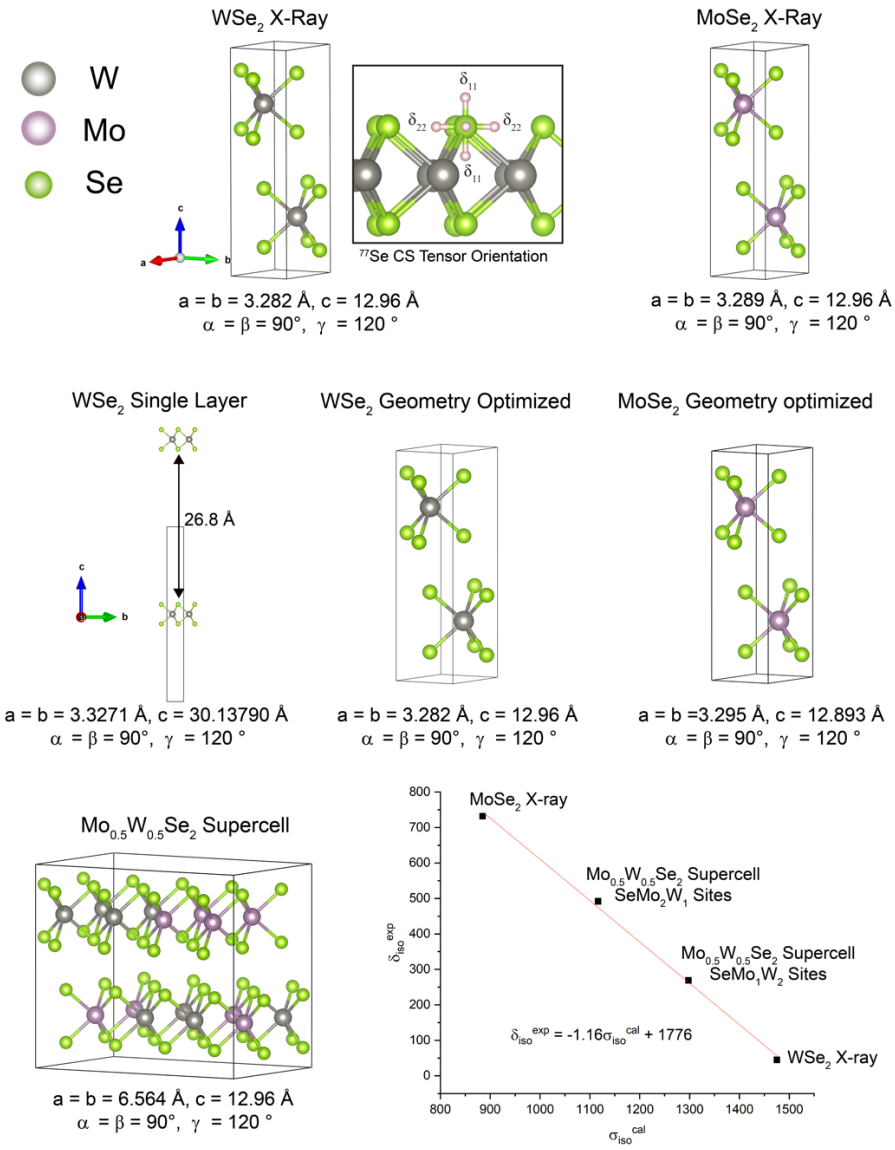

Figure S13. Crystal structures used for plane-wave DFT calculations on WSe_2 and $MoSe_2$. The unit cell parameters before and after geometry optimization (relaxation) are indicated. For WSe_2, the orientation of the ^{77}Se chemical shift tensor is shown in the molecular frame (δ_{33} out of the page). Calculations were also performed on a WSe_2 single layer to investigate the effect or removing adjacent TMDC layers on the calculated chemical shift. The single layer model was obtained by increasing the inter-layer Se-Se distance to 26.8 Å. A fully relaxed super-cell representing the stoichiometry $Mo_{0.5}W_{0.5}Se_2$ is shown at the bottom. The ordering of the Mo and W atoms was varied in both layers to give all possible permutations of Se coordination environments ($SeMo_3$, $SeMo_2W$, $SeMoW_2$, and SeW_3). The calibration curve used for conversion of shielding to shift values is shown in the lower right corner.

Table S3. GIPAW calculated ^{77}Se shielding values for the $Mo_{0.5}W_{0.5}Se_2$ supercell.[a]

Se Site	σ_{33} (ppm)	σ_{22} (ppm)	σ_{11} (ppm)	σ_{iso} (ppm)	δ_{iso} (ppm)
SeW_3	1622.1	1605.5	1171.6	1466.4	
	1621.8	1605.3	1171.4	1466.2	
	1617.4	1607.9	1171.2	1465.5	
	1617.0	1607.6	1171.0	1465.2	
Average	*1619.6*	*1606.6*	*1171.3*	*1465.8*	*75.7*
$SeMoW_2$	1605.9	1418.6	849.2	1291.2	
	1605.4	1418.5	849.2	1291.0	
	1598.8	1398.0	920.2	1305.7	
	1598.7	1397.9	920.0	1305.6	
	1597.1	1397.4	887.5	1294.0	
	1596.9	1397.2	887.2	1293.8	
	1589.2	1424.4	884.6	1299.4	
	1589.1	1424.4	884.5	1299.3	
	1586.3	1417.1	889.8	1297.7	
	1585.8	1417.0	889.9	1297.5	
	1583.8	1422.1	890.5	1298.8	
	1583.4	1422.0	890.6	1298.6	
	1578.3	1403.8	916.6	1299.6	
	1578.2	1403.8	916.5	1299.5	
Average	*1591.2*	*1411.6*	*891.2*	*1298.0*	*270.3*
$SeMo_2W$	1475.4	1293.9	616.7	1128.7	
	1474.7	1293.8	616.9	1128.5	
	1465.5	1272.4	605.5	1114.5	
	1464.7	1272.1	605.6	1114.1	
	1462.0	1294.5	588.0	1114.8	
	1461.9	1294.6	587.8	1114.8	
	1442.9	1296.0	585.1	1108.0	
	1442.6	1295.7	585.3	1107.9	
Average	*1461.2*	*1289.1*	*598.9*	*1116.4*	*481.0*
$SeMo_3$	1221.1	1206.0	255.7	894.2	
	1221.0	1205.8	255.9	894.2	
	1218.7	1206.0	301.2	908.6	
	1218.2	1205.9	301.8	908.6	
	1210.5	1188.4	294.1	897.7	
	1209.9	1187.8	294.6	897.4	
Average	*1216.6*	*1200.0*	*283.9*	*900.1*	*731.8*

[a]See Table 2 of the main manuscript for the average calculated chemical shift tensor parameters for each Se site.

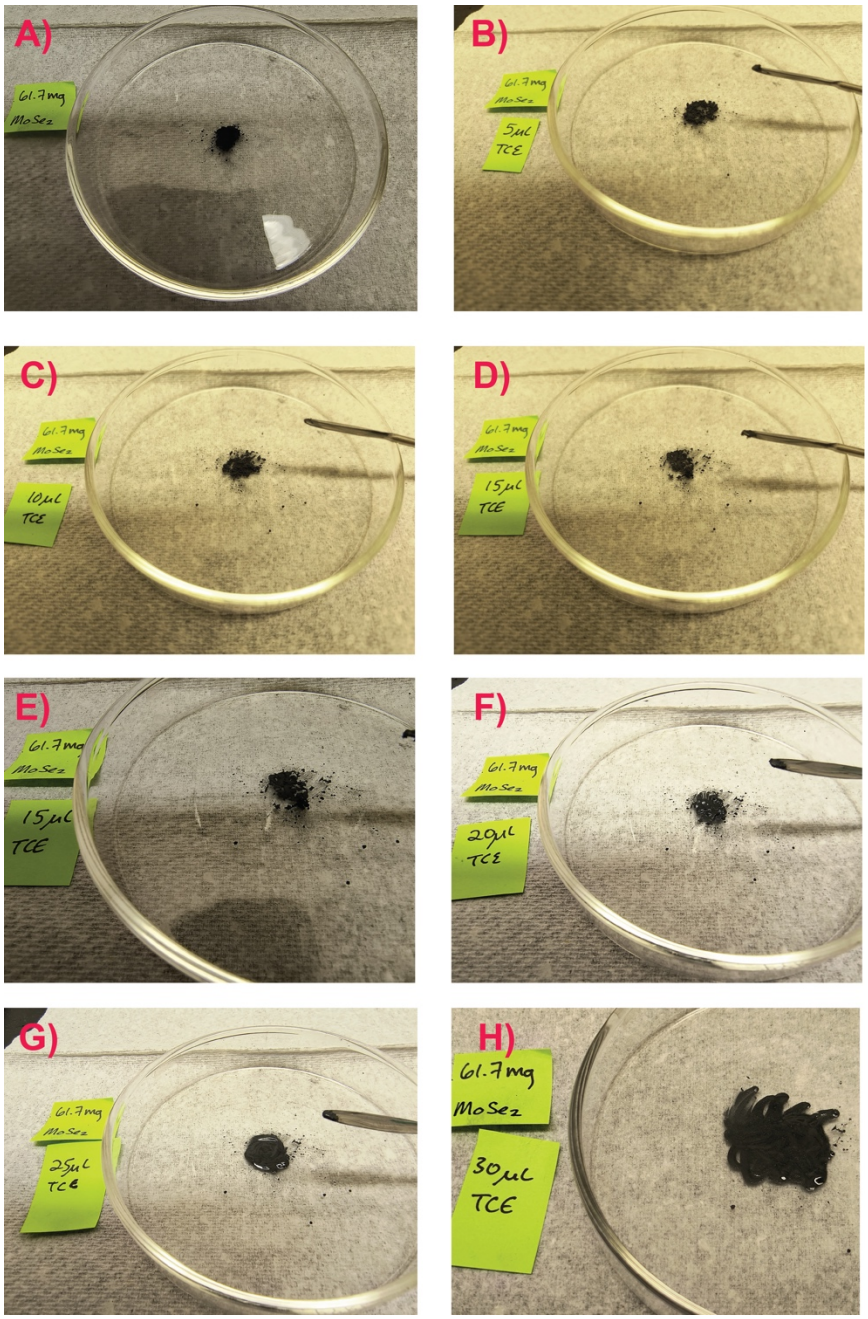

Figure S14. Photographs illustrating the effects of impregnating 61.7 mg of $MoSe_2$ with different amounts of tetrachloroethane (TCE). 5 μL of TCE was added to the $MoSe_2$ each time to increase the total volume. Up until the addition of 20 μL the sample maintains its powder consistency. After addition of 25 mL of TCE, the sample begins to dissolve or disperse. (A) 61.7 mg of $MoSe_2$ without any solvent added. (B) $MoSe_2$ after addition of 5 μL of TCE. (C) 10 μL of TCE added. (D, E) 15 μL of TCE added. The second image was taken about 1 minute after addition of the TCE. (F) 20 μL of TCE added. (G) 25 μL of TCE added. (H) 30 μL of TCE added.

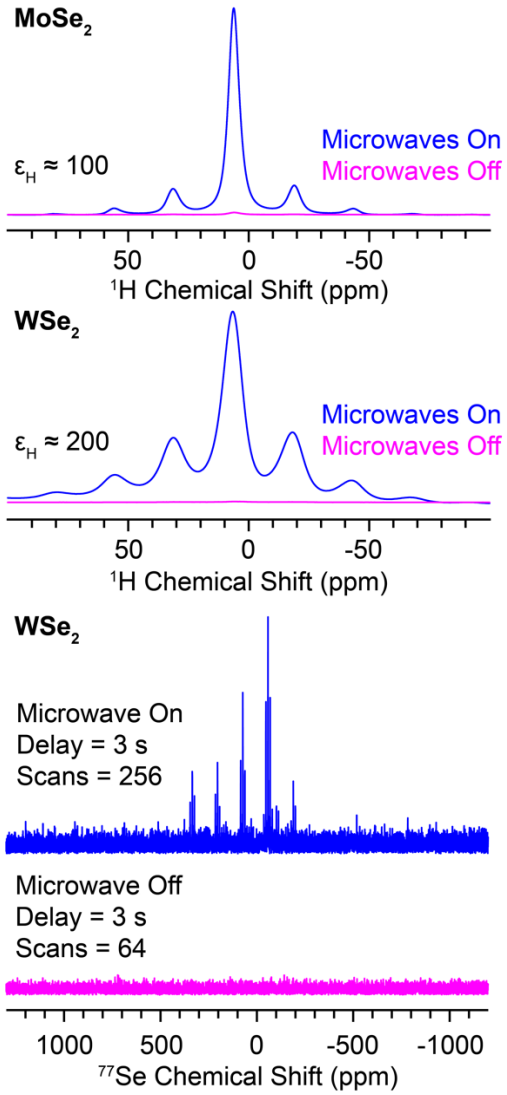

Figure S15. MAS ^{1}H spin echo SSNMR spectra of the $MoSe_2$ and WSe_2 samples impregnated with TEKPol tetrachloroethane solution. The ^{1}H SSNMR spectra are shown with (blue) and without (pink) microwave irradiation. The ^{1}H DNP enhancement is indicated and was determined by comparing the intensity of the spectra with and without microwave irradiation. ^{1}H→^{77}Se CP-CPMG NMR spectra of WSe_2 are shown with and without microwave irradiation. The number of scans and recycle delay is indicated. The sample temperature was approximately 110 K and the MAS frequency was 10 kHz for all SSNMR experiments.

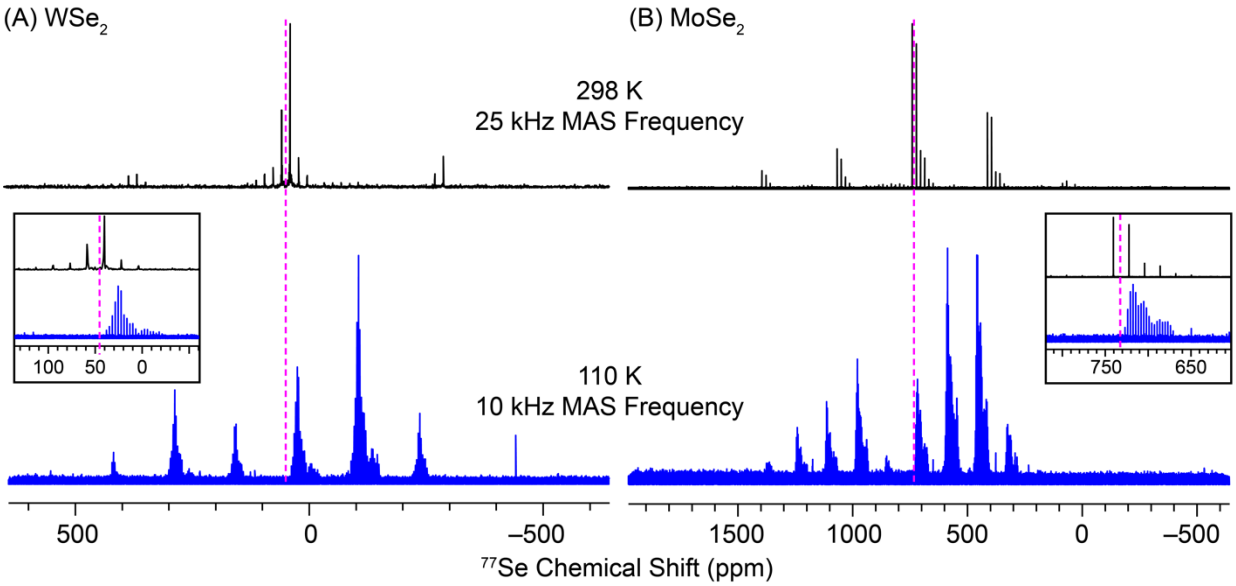

Figure S16. Comparison of MAS ^{77}Se SSNMR spectra obtained with temperatures of 298 K and 110 K for (A) WSe_2 and (B) $MoSe_2$. Insets show expanded views of the isotropic peaks. Dashed vertical lines indicate the 298 K isotropic chemical shifts. The 110 K MAS SSNMR spectra were obtained with 3.2 mm rotors. 16 scans were averaged and the recycle delay was 1000 s.

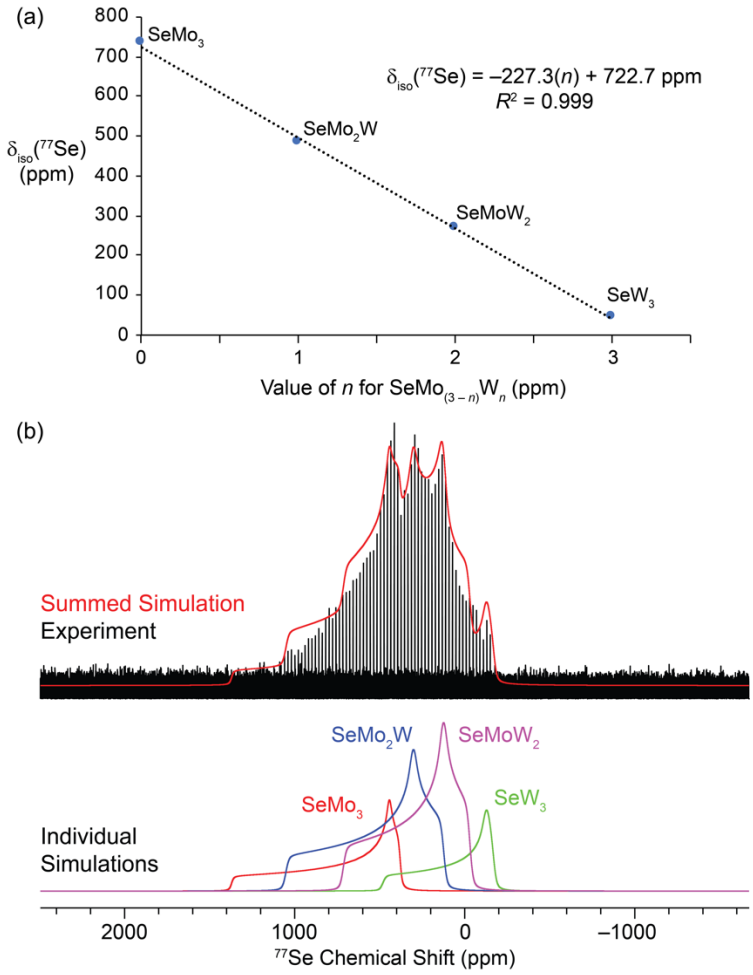

Figure S17. (a) A plot of experimental isotropic ^{77}Se chemical shifts as a function of the number of W atoms bonded to Se (*n*). The shift of each type of Se site is indicated. (b) Experimental and simulated static ^{77}Se solid-state NMR spectrum of ball milled and annealed $Mo_{0.5}W_{0.5}Se_2$. The simulated spectrum (red) is overlaid on the experimental spectrum (black). The simulated shielding patterns for the four Se sites are shown below.

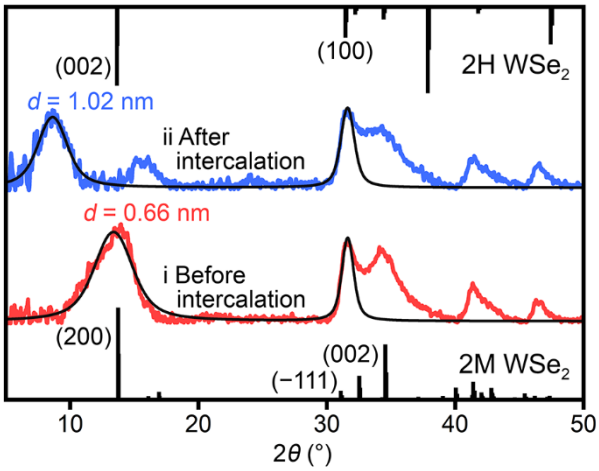

Figure S18. PXRD patterns of WSe_2 nanocrystals (i) before and (ii) after intercalation of ethylenediamine. Overlaid traces show Voigt fits in the ranges of 5–15 ° and 30–32 °. Patterns predicted from single-crystal data for 2M[S7] (bottom) and 2H[S8] (top) WSe_2 are shown for reference.

Table S4. Reflection positions (μ), FWHM, and corresponding Scherrer domain sizes of WSe_2 nanocrystals before and after intercalation with $Et(NH_2)_2$.

	Interlayer Reflection		$2\theta \approx 31.6$ °		Domain size along stacking direction (nm)	Number of Layers	~Lateral Domain Size (nm)
	μ (°)	FWHM (°)	μ (°)	FWHM (°)			
Before intercalation	13.39	3.575	31.63	1.095	3.4	5.1	15
After intercalation	8.64	2.745	31.62	1.270	4.9	4.8	13

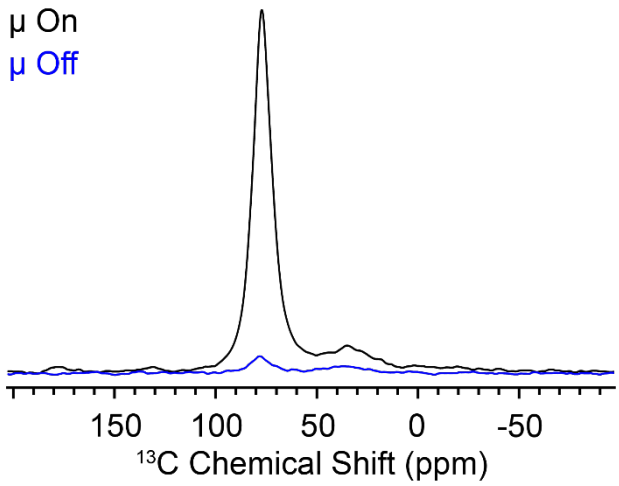

Figure S19. ^{13}C CPMAS SSNMR spectra of ethylenediamine-intercalated WSe_2 nanocrystals impregnated with TEKPol tetrachloroethane (TCE) solution. The CPMAS DNP enhancement ($e_{C\ CP}$) was approximately 20 for the TCE ^{13}C NMR signal and $e_{C\ CP}$ was approximately 4 for the alkyl signal of the intercalated ethylenediamine.

Table S5. Amounts of chemicals used in the syntheses of WSe_2 nanocrystals.

$W(CO)_6$ (g)	$W(CO)_6$ (mmol)	Oleic acid (g)	Oleic acid (mmol)	TOPO (g)	Ph_2Se_2 (g)	Ph_2Se_2 (mmol)	Hexadecane (g)
0.0199	0.0565	1.6162	5.7217	5.0723	0.0355	0.114	0.7730
0.0206	0.0585	1.6313	5.7751	5.0148	0.0356	0.114	0.7730

Table S6. Experimental solid-state NMR parameters.

Figure	Experiment	MAS Frequency (kHz)	Recycle Delay (s) (D1)	Scans	Probe	Rotor diameter (mm)	Experiment Time
Figure 4A (Top)	WURST-CPMG	-	1000	128	4 mm HX	4	35.6 h
Figure 4A (Bottom)	CPMG	25	1000	128	2.5 mm MAS HX	2.5	35.6 h
Figure 4B (top)	WURST-CPMG	-	1000	128	4 mm HX	4	35.6 h
Figure 4B (bottom)	CPMG	25	1000	32	2.5 mm MAS HX	2.5	9 h
Figure 5 Left (top)	CP-CPMG	10	3	256	3.2 mm DNP MAS HX	3.2	13.7 min.
Figure 5 Left (middle)	CP-Pulse cooling	10	51	17	3.2 mm DNP MAS HX	3.2	54.4 min.
Figure 5 Left (bottom)	CPMG	25	1000	48	2.5 mm MAS HX	2.5	13.3 h
Figure 5 Right (top)	CP-CPMG	10	3.5	1024	3.2 mm MAS HX	3.2	1 h
Figure 5 Right (middle)	CP-Pulse cooling	10	36	1024	3.2 mm MAS HX	3.2	10.2 h
Figure 5 Right (bottom)	CPMG	25	1000	32	2.5 mm MAS HX	2.5	8.9 h
Figure 6 Left (pure WSe_2)	CPMG	25	1000	128	2.5 mm MAS HX	2.5	35.6 h
Figure 6 Left (milled $MoSe_2$ + WSe_2)	CPMG	25	50	512	2.5 mm MAS HX	2.5	7.5 h
Figure 6 Left (milled, annealed $MoSe_2$ + WSe_2)	CPMG	25	1000	32	2.5 mm MAS HX	2.5	9 h

Figure 6 Left (milled MoS_2 + WSe_2)	CPMG	25	50	512	2.5 mm MAS HX	2.5	7.5 h
Figure 6 Left (milled, annealed MoS_2 + WSe_2)	CPMG	25	1000	32	2.5 mm MAS HX	2.5	9 h
Figure 6 Left (pure $MoSe_2$)	CPMG	25	1000	32	2.5 mm MAS HX	2.5	9 h
Figure 6 Right (pure WSe_2)	WURST-CPMG	-	1000	128	4 mm HX	4	35.6 h
Figure 6 Right (physical mixture $MoSe_2$ + WSe_2)	WURST-CPMG	-	1000	64	4 mm HX	4	18 h
Figure 6 Right (annealed $MoSe_2$ + WSe_2)	WURST-CPMG	-	1000	128	4 mm HX	4	35.6 h
Figure 6 Right (milled $MoSe_2$ + WSe_2)	WURST-CPMG	-	50	2048	4 mm HX	4	31.5 h
Figure 6 Right (milled, annealed $MoSe_2$ + WSe_2)	WURST-CPMG	-	1000	2048	4 mm HX	4	71.5 h
Figure 6 Right (milled, annealed MoS_2 + WSe_2)	WURST-CPMG	-	500	256	4 mm HX	4	36 h
Figure 6 Right (milled	WURST-CPMG	-	50	2048	4 mm HX	4	31.5 h

MoS_2 + WSe_2)							
Figure 6 Right (annealed MoS_2 + WSe_2)	WURST-CPMG	-	1000	128	4 mm HX	4	36 h
Figure 6 Right (physical mixture MoS_2 + WSe_2)	WURST-CPMG	-	1000	64	4 mm HX	4	18 h
Figure 6 Right (pure $MoSe_2$)	WURST-CPMG	-	1000	128	4 mm HX	4	35.6 h
Figure 7 (top)	CP-CPMG	10	2.6	18432	3.2 mm MAS HX	3.2	13.5 h
Figure 7 (bottom)	CP-Spin echo	10	3	32	3.2 mm MAS HX	3.2	3 min.
Figure S9 left (top)	WURST-CPMG	-	400	8	4 mm HX	~ 5	53 min.
Figure S9 left (bottom)	WURST-CPMG	-	400	16	4 mm HX	~ 5	107 min.
Figure S9 right (top)	WURST-CPMG	-	1000	16	4 mm HX	~ 5	4.5 h
Figure S11 (top)	CPMG	25	1000	128	2.5 mm MAS HX	2.5	35.6 h
Figure S11 (middle)	CPMG	10	1000	48	4 mm MAS HX	4	13.4 h
Figure S11 (bottom)	CPMG	10	1000	48	4 mm MAS HX	4	13.4 h
Figure S14 WSe_2 (microwave on)	CP-CPMG	10	3	256	3.2 mm MAS HX	3.2	13 min.
	CP-CPMG	10	3	64	3.2 mm MAS HX	3.2	3 min.

Supporting Information References

[S1] Gusakova, J.; Wang, X.; Shiau, L.L.; Krivosheeva, A.; Shaposhnikov, V.; Borisenko, V.; Gusakov, V.; Tay, B.K. Electronic Properties of Bulk and Monolayer TMDs: Theoretical Study within DFT Framework (GVJ-2e Method). *Phys. Status Solidi (a)*, **2017**, *214*(12), 1700218.

[S2] Zollner, K.; Junior, P.E.F.; Fabian, J. Strain-Tunable Orbital, Spin-Orbit, and Optical Properties of Monolayer Transition-Metal Dichalcogenides. *Phys. Rev. B* **2019**, *100*(19), 195126.

[S3] Kam, K.K.; Parkinson, B.A. Detailed Photocurrent Spectroscopy of the Semiconducting Group VIB Transition Metal Dichalcogenides. *J. Phys. Chem.* **1982**, *86*(4), 463–467.

[S4] Kuc, A.; Zibouche, N.; Heine, T. Influence of Quantum Confinement on the Electronic Structure of the Transition Metal Sulfide TS_2. *Phys. Rev. B* **2011**, *83* (24), 245213.

[S5] Tongay, S.; Zhou, J.; Ataca, C.; Lo, K.; Matthews, T.S.; Li, J.; Grossman, J.C.; Wu, J. Thermally Driven Crossover from Indirect toward Direct Bandgap in 2D Semiconductors: $MoSe_2$ versus MoS_2. *Nano Lett.* **2012**, *12* (11), 5576–5580.

[S6] Li, W.; Walther, C.F.; Kuc, A.; Heine, T. Density Functional Theory and Beyond for Band-Gap Screening: Performance for Transition-Metal Oxides and Dichalcogenides. *J. Chem. Theory Comput.* **2013**, *9* (7), 2950–2958.

[S7] Fang, Y.; Dong, Q.; Pan, J.; Liu, H.; Liu, P.; Sun, Y.; Li, Q.; Zhao, W.; Liu, B.; Huang, F. Observation of Superconductivity in Pressurized 2M WSe_2 Crystals. *J. Mater. Chem. C* **2019**, *7* (28), 8551–8555.

[S8] Schutte, W. J.; De Boer, J. L.; Jellinek, F. Crystal Structures of Tungsten Disulfide and Diselenide. *J. Solid State Chem.* **1987**, *70* (2), 207–209.